



UNIVERSITY OF LEEDS

This is a repository copy of *Magnetic fabrics reveal three-dimensional flow processes within elongate magma fingers at the margin of the Shonkin Sag laccolith (MT, USA)*.

White Rose Research Online URL for this paper:

<https://eprints.whiterose.ac.uk/196631/>

Version: Accepted Version

Article:

Köpping, J, Cruden, AR, Magee, C orcid.org/0000-0001-9836-2365 et al. (3 more authors) (2023) Magnetic fabrics reveal three-dimensional flow processes within elongate magma fingers at the margin of the Shonkin Sag laccolith (MT, USA). *Journal of Structural Geology*, 169. 104829. ISSN 0191-8141

<https://doi.org/10.1016/j.jsg.2023.104829>

© 2023, Elsevier. This manuscript version is made available under the CC-BY-NC-ND 4.0 license <http://creativecommons.org/licenses/by-nc-nd/4.0/>.

Reuse

This article is distributed under the terms of the Creative Commons Attribution-NonCommercial-NoDerivs (CC BY-NC-ND) licence. This licence only allows you to download this work and share it with others as long as you credit the authors, but you can't change the article in any way or use it commercially. More information and the full terms of the licence here: <https://creativecommons.org/licenses/>

Takedown

If you consider content in White Rose Research Online to be in breach of UK law, please notify us by emailing eprints@whiterose.ac.uk including the URL of the record and the reason for the withdrawal request.



eprints@whiterose.ac.uk
<https://eprints.whiterose.ac.uk/>

1 Magnetic fabrics reveal three-dimensional flow processes within
2 elongate magma fingers at the margin of the Shonkin Sag
3 laccolith (MT, USA)

4 **Jonas Köpping^{1*}, Alexander R. Cruden¹, Craig Magee², William McCarthy³, John**
5 **Geissman^{4,5}, Daniel Holm⁶**

6

7 *¹School of Earth, Atmosphere and Environment, Monash University, Melbourne, 3800, Australia*

8 *² School of Earth and Environment, University of Leeds, Leeds, LS2 9JT, UK*

9 *³School of Earth and Environmental Sciences, University of St. Andrews, UK*

10 *⁴ Department of Geosciences, University of Texas at Dallas, Richardson, TX 75080, USA*

11 *⁵ Department of Earth and Planetary Sciences, University of New Mexico, Albuquerque, NM*
12 *87131, USA*

13 *⁶ Department of Geology, Kent State University, Kent, Ohio 44242, USA*

14

15 **Corresponding author: Jonas Köpping, jonas.koepping@erdw-ethz.ch*

16

17 **Abstract**

18 Unravelling magma flow in ancient sheet intrusions is critical to understanding how magma
19 pathways develop and feed volcanic eruptions. Analyzing the shape preferred orientation of
20 minerals in intrusive rocks can provide information on magma flow, because crystals may align
21 parallel to the primary flow direction. Anisotropy of magnetic susceptibility (AMS) is an
22 established method to quantify such shape preferred orientations in igneous sheet intrusions with
23 weak or cryptic fabrics. However, use of AMS data to characterize how magma flows within the
24 individual building blocks of sheet intrusions (i.e., magma fingers and segments), hereafter
25 referred to as elements, has received much less attention. Here we use a high spatial resolution
26 sampling strategy to quantify the AMS fabric of the Eocene Shonkin Sag laccolith (Montana,
27 USA) and associated elongate magma fingers. Our results suggest that magnetic fabrics across the
28 main laccolith reflect sub-horizontal magma flow, and inferred flow directions are consistent with
29 an underlying NE-SW striking feeder dyke. Within the magma fingers, we interpret systematic
30 changes in magnetic fabric shape and orientation to reflect the interaction between competing
31 forces occurring during along-finger magma flow (i.e., simple shear) and horizontal and vertical
32 inflation (i.e., pure shear flattening). For example, we highlight local crossflow of magma between
33 coalesced fingers increases the complexity of magma flow kinematics and related fabrics. Despite
34 these complexities, the AMS data in coalesced magma fingers maintain their internal flow- and
35 inflation-related fabrics, which suggests that magma flow within the fingers remains channelized
36 after coalescence. Given that many sheet intrusions consist of amalgamated elements, our findings
37 highlight the need to carefully consider element distribution and sample locations when
38 interpreting magma flow based on AMS measurements.

39

40 1. Introduction

41 Magma transport in the Earth's upper crust is facilitated by networks of interconnected sheet
42 intrusions (i.e., sills and dykes) (e.g., Anderson, 1937, 1951; Elliot and Fleming, 2004; Leat, 2008;
43 Muirhead et al., 2012; Magee et al., 2016a; Schofield et al., 2017; Eide et al., 2021). These sills
44 and dykes commonly form via the coalescence of discrete, laterally restricted elements, such as
45 magma fingers and segments (Fig. 1; e.g., Pollard et al., 1975; Rickwood, 1990; Horsman et al.,
46 2005; Schofield et al., 2012b; Galland et al., 2019; Magee et al., 2019; Stephens et al., 2021;
47 Köpping et al., 2022): magma fingers have pipe-like geometries with large thickness-to-width
48 ratios of $\sim 0.1\text{--}1$ and rounded intrusion tips, whereas segments have blade-like geometries with
49 relatively small thickness-to-width ratios of $\sim <0.1$ and sharp intrusion tips (see Magee et al., 2019
50 and references therein). Both magma fingers and segments are elongated parallel to their
51 propagation direction, such that their long axes are a proxy for the primary magma flow direction
52 (e.g., Pollard et al., 1975; Schofield et al., 2012; Galland et al., 2019).

53 Previous studies of sheet intrusion elements have focused on their 3-D geometry and the host rock
54 deformation mechanisms that accommodate their emplacement and growth (e.g., Pollard et al.,
55 1975; Schofield et al., 2012a; Spacapan et al., 2017; Stephens et al., 2021; Köpping et al., 2022).
56 However, few studies have examined how the formation and coalescence of elements impacts
57 internal magma flow kinematics (Horsman et al., 2005; Magee et al., 2013, 2016b). Yet
58 deciphering how magma flows within elements, and whether it mixes or remains channelized when
59 elements coalesce, is critical to understanding: (1) the formation and architecture of both sheet
60 intrusions and upper-crustal magma plumbing systems (e.g., Muirhead et al., 2012; Magee et al.,
61 2016a; Schofield et al., 2017); (2) the subsurface distribution of magma and its impact on potential
62 eruption locations and volcanic hazards (e.g., Sparks, 2003; Cashman and Sparks, 2013); and (3)

63 formation of many Ni-Cu-PGE sulfide deposits, which commonly accumulate in areas of high
64 magma flux within restricted magma channels such as elongate intrusions (e.g., tubular chonoliths)
65 (e.g., Barnes et al., 2016).

66 [Insert Figure 1 here.]

67 Reconstructing magma flow in sheet intrusions is often accomplished using anisotropy of magnetic
68 susceptibility (AMS) analyses, which are widely used for quantifying the average magnetic fabric
69 of a rock sample (e.g., Knight and Walker, 1988; Tarling and Hrouda, 1993; Philpotts and Asher,
70 1994; Cruden et al., 1999; Ferré et al., 2002; Tauxe, 2003; Poland et al., 2004; Horsman et al.,
71 2005; Morgan et al., 2008; McCarthy et al., 2015; Andersson et al., 2016; Magee et al., 2016b;
72 Martin et al., 2019). These analyses are reliant on the preservation of magma flow patterns by the
73 orientation of crystals during emplacement (REF). Yet magnetic fabrics and their equivalent
74 petrofabrics can be modified and overprinted by syn- and post-emplacement tectonic deformation,
75 and by changing internal flow and crystallization processes (e.g., during element coalescence),
76 which may complicate how they are interpreted (e.g., Riller et al., 1996; Andersson et al., 2016;
77 Mattsson et al., 2018; Burchardt et al., 2019; Burton-Johnson et al., 2019; Martin et al., 2019).
78 Furthermore, because parts of an intrusion (e.g., an element) may solidify and lock in fabrics with
79 different orientations at different times during emplacement, it is likely that a range of processes,
80 from initial propagation to inflation and potential late-stage backflow, will be recorded by fabrics
81 within an intrusion (e.g., Philpotts and Philpotts, 2007). Given this potential variation in fabric
82 orientation, a key limitation in previous magma flow studies, particularly of tabular intrusions, is
83 that because sample locations are commonly widely distributed along the intrusion plane, they
84 may record different and unrelated processes. High-resolution sampling strategies are therefore
85 necessary to unravel the flow history of sheet intrusions in cross-sectional outcrops (e.g., Cañón-

86 Tapia and Herrero-Bervera, 2009; Magee et al., 2013, 2016b; Andersson et al., 2016; Morgan et
87 al., 2017; Martin et al., 2019). Although some AMS studies with high-resolution sampling
88 strategies have been conducted in sheet intrusions that likely comprise coalesced elements, the
89 internal flow kinematics within elongate pipe-like elements remain uncertain (Magee et al., 2016b;
90 Hoyer and Watkeys, 2017; Martin et al., 2019). There are likely two competing emplacement
91 mechanisms that will control the orientation and shape of fabrics in elements: (1) alignment of
92 crystals broadly parallel to the magma flow, defined by an axially symmetric, parabolic velocity
93 profile, assuming laminar Poiseuille flow (e.g., Leite, 1959; Knight and Walker, 1988) (Figs. 2A–
94 2B); and (2) flattening of fabrics against the walls during magma finger inflation (e.g., Merle,
95 2000) (Fig. 2B). Initial fabrics are likely to be flow related but may be modified and overprinted
96 by pure shear flattening strain during intrusion growth (e.g., Merle, 2000). It is important to note
97 that fabrics recorded in AMS data reflect the strain at the time of local magma solidification during
98 magma emplacement. Therefore, the effect of each individual emplacement mechanism on both
99 fabric orientation and shape as well as the amount of fabric overprinting may vary between
100 individual sample locations.

101 Here, we present AMS and petrofabric data from both the main Shonkin Sag laccolith, Montana,
102 USA (e.g., Weed and Pirsson, 1895; Pirsson, 1905; Osborne and Roberts, 1931; Barksdale, 1937;
103 Hurlbut Jr, 1939; Kendrick and Edmond, 1981; Ruggles et al., 2021), and discrete and coalesced,
104 well-exposed elongate magma fingers that emerge from the laccolith's southeast margin (Fig. 3)
105 (Pollard et al., 1975). The southeast margin exposure represents an ideal study location because
106 the magma fingers have a well-defined long axis, equivalent to the primary magma flow direction,
107 and are easily accessed for high-resolution sampling (Pollard et al., 1975). By combining AMS
108 and petrofabric analyses of samples collected from the Shonkin Sag laccolith and its marginal

109 magma fingers, this study aims to investigate: (1) potential emplacement and flow kinematics of
110 the Shonkin Sag laccolith; (2) whether magnetic fabrics in both discrete and coalesced magma
111 fingers reflect primary magma flow; (3) if flow in two coalesced fingers was sheet-like (i.e.,
112 magma mixed) and the coalesced fingers behaved as one body, or if flow remained localized within
113 individual fingers; and (4) any potential differences and similarities between magnetic fabrics
114 within the Shonkin Sag laccolith and its marginal magma fingers.

115 A combination of regional mapping (Montana Bureau of Mines and Geology, 2021) and magnetic
116 fabric analyses suggests that the Shonkin Sag laccolith was fed by an underlying NE-SW striking
117 dyke and that fabrics recorded within both discrete and coalesced magma fingers reflect an
118 interplay of along-finger magma flow and horizontal and vertical inflation. Local crossflow of
119 magma may occur where fingers coalesce; however, fabrics observed in most areas of coalesced
120 magma fingers maintain their internal flow- and inflation-related fabrics, which suggests that
121 magma flow within the fingers remains channelized after coalescence. Understanding where
122 magma flow channelizes in igneous sheet intrusions provides a better understanding of internal
123 magma transport and intrusion growth processes, which is important for improving knowledge on
124 the architecture of both sheet intrusions and trans-crustal magma plumbing systems. Channelized
125 magma flow further locally increases the magma flux, which enhances the potential for thermal-
126 mechanical erosion of surrounding host rocks and subsequent incorporation of host rock xenoliths
127 into the magma (e.g., Barnes et al., 2016). This process contributes to making space for the
128 intruding magma and increases its crustal sulfur content, leading to the formation of economically
129 significant Ni-Cu-PGE deposits (e.g., Uitkomst Complex) (e.g., Gauert et al., 1996; Barnes et al.,
130 2016). Identifying areas of channelized magma flow within sheet intrusions therefore has
131 implications for Ni-Cu-PGE exploration.

132

133 **2. Geological setting**

134 Cenozoic felsic and mafic igneous intrusive and volcanic rocks of the Highwood Mountains are
135 part of the Central Montana alkalic province (Figs. 3A–3B) (Weed and Pirsson, 1895; Pirsson,
136 1905; Barksdale, 1937; Hurlbut Jr, 1939; Buie, 1941; Burgess, 1941; Pollard et al., 1975; Kendrick
137 and Edmond, 1981; Henderson et al., 2012). The early Eocene ($\sim 52 \pm 1$ Ma) formation of the
138 Highwood Mountains occurred in two stages: (1) volcanic eruptions, which emplaced both quartz
139 latite flows and silicic pyroclastic rocks; and (2) later volcanism with mafic phonolite flows (e.g.,
140 Hurlbut Jr, 1939; Burgess, 1941; Larsen, 1941; O’Brien et al., 1991). Mafic igneous intrusions
141 linked to the second stage of volcanism include a radial dyke swarm surrounding the main volcanic
142 complex, as well as sills, laccoliths, and chonoliths that have a range of magma compositions (e.g.,
143 shonkinite, syenite, biotite pyroxenite) (Figs. 3B–3C) (e.g., Hurlbut Jr, 1939; Buie, 1941; Burgess,
144 1941; Larsen, 1941; Nash and Wilkinson, 1970, 1971; O’Brien et al., 1991; Henderson et al.,
145 2012).

146 [Insert Figure 2 here.]

147 The samples used in this study were collected from the Shonkin Sag laccolith, a ~ 51 Ma old, ~ 70
148 m thick, sub-circular sheet intrusion with a diameter of ~ 2.3 – 3 km (Fig. 3B) (e.g., Barksdale, 1937;
149 Marvin et al., 1980). Five sills (No 1–5) emerge from the southeast margin of the laccolith; at a
150 distance of >266 m from the laccolith edge, three of these sills split into elongate magma fingers
151 (Fig. 3D) (Pollard et al., 1975). The main Shonkin Sag laccolith is characterized by layering of
152 shonkinite and syenite. This layering has been the subject of a number of petrologic studies for
153 over a century, with debate focusing on whether the igneous layering formed by differentiation of

154 a single magma pulse or by injection of multiple magma pulses (e.g., Pirsson, 1905; Osborne and
155 Roberts, 1931; Barksdale, 1937; Hurlbut Jr, 1939; Kendrick and Edmond, 1981; Ruggles et al.,
156 2021). Based on magnetic fabric measurements, structural analysis and thermal modelling,
157 Ruggles et al. (2021) suggest that the Shonkin Sag laccolith was emplaced via at least seven
158 discrete magma pulses over a period of ca. 3 years, while subsequent differentiation and
159 solidification of the laccolith may have occurred over ca. 21 years. Most of the laccolith and all of
160 the igneous sills that emerge from its southeast margin are made of porphyritic shonkinite with
161 clinopyroxene, olivine, and (pseudo)leucite phenocrysts hosted in a fine-to-medium grained
162 groundmass of biotite, clinopyroxene, and olivine (e.g., Pirsson, 1905; Osborne and Roberts, 1931;
163 Barksdale, 1937; Hurlbut Jr, 1939; Nash and Wilkinson, 1970; Kendrick and Edmond, 1981;
164 Henderson et al., 2012; Ruggles et al., 2021). Ruggles et al. (2021) identified magnetite as the
165 dominant magnetic mineral associated with magnetic fabrics at the margin of the laccolith and
166 within the sills. Here we focus on magnetic fabrics and petrofabrics within elongate, SE trending
167 magma fingers, which emerge from the sills located at the SE laccolith margin (Fig. 3D) (Pollard
168 et al., 1975). These fingers are of meter-scale with thickness-to-width ratios of 0.1–0.83 and they
169 crop out in a large main cliff face, and in multiple blocks detached from the cliff (Fig. 3D,
170 Supplemental Material S0) (Pollard et al., 1975). The detached blocks remain upright and have not
171 been transported far, so we can map individual magma fingers across them to study the 3D finger
172 geometry (Pollard et al., 1975).

173 **3. Methods and background**

174 *3.1. Sample location and preparation*

175 Samples were collected from twenty-three locations at varying elevation levels across the Shonkin
176 Sag laccolith and from twenty-one locations within two discrete and two coalesced magma fingers
177 at the SE laccolith margin (sample locations are given in Supplemental Material S1). Based on
178 their clustered spatial location, samples collected from the interior of the laccolith were divided
179 into four groups, located NNE, W, SW, and S of the geographic laccolith center (referred to as
180 SSL-1, SSL-2, SSL-3, and SSL-4, respectively). The two coalesced magma fingers, named Hb and
181 Hc, and the discrete magma fingers, named II and JJ, emerge from sill No. 5 and are located ~305
182 m and ~500 m east of the laccolith-sill-transition, respectively (Fig. 3D). Samples collected from
183 magma fingers are labeled by the finger ID and a continuous number (e.g., II-1, II-2, II-3, etc...).
184 In order to use magnetic fabrics and petrofabrics to assess potential magma flow kinematics within
185 the magma fingers, we collected oriented sample cores from: (1) the finger centers; (2) close to
186 the top and bottom finger margins; and (3) close to the lateral tips of each magma finger. For the
187 two coalesced fingers Hb and Hc, additional samples were collected from the step that connects
188 the vertically offset fingers. Samples were collected away from the quenched, mm- to cm-thick,
189 highly-fractured, glassy margin that surrounds many of the magma fingers. All collected samples
190 were cut into ~2.2 cm long cylinders resulting in 262 specimens and an average of eleven
191 specimens per sample location across the main laccolith, and 127 specimens and an average of six
192 specimens per sample location within the magma fingers.

193

194 3.2. *Magnetic fabric analyses*

195 The AMS fabrics of specimens collected from the interior of the Shonkin Sag laccolith were
196 measured using an AGICO KLY-3S Kappabridge at the University of New Mexico, with a

197 magnetic field of 423 m/A and a frequency of 875 Hz. Specimens collected from the magma
198 fingers were analyzed using an AGICO KLY5 Kappabridge with an attached 3-D-rotator in the
199 M³Ore Lab at the University of St. Andrews. Analyses were conducted using a magnetic field of
200 400 m/A and a frequency of 1220 Hz.

201 The magnetic susceptibility (K) of each analyzed specimen is described by a second-rank tensor,
202 which is commonly visualized as a magnitude ellipsoid with the principal eigenvectors, or
203 susceptibilities, K_1 , K_2 , and K_3 being the maximum, intermediate, and minimum axes of the
204 ellipsoid, respectively (e.g., Khan, 1962; Hrouda, 1982). Where AMS ellipsoids have a prolate
205 shape ($K_1 > K_2 \simeq K_3$), K_1 may be interpreted to represent the magma flow or stretching direction,
206 whereas oblate fabrics ($K_1 \simeq K_2 > K_3$) may represent the magma flow or stretching/imbrication
207 plane (K_1 - K_2 plane) (e.g., Knight and Walker, 1988; Cruden and Launeau, 1994; Tauxe et al.,
208 1998). Notably, for imbricated fabrics, the imbrication closure has been interpreted to point in the
209 direction of magma transport (Fig. 2A) (e.g., Knight and Walker, 1988; Philpotts and Philpotts,
210 2007). The mean, or bulk, susceptibility (K_m) of an AMS ellipsoid is defined as:

$$K_m = \frac{K_1 + K_2 + K_3}{3} \quad (1)$$

211 and is measured in SI units. Additional parameters that describe the AMS ellipsoid include the
212 dimensionless corrected anisotropy degree (P_j) and the shape parameter (T) (Jelinek, 1981). The
213 corrected anisotropy degree is:

$$P_j = \exp\sqrt{2[(\eta_1 - \eta_m)^2 + (\eta_2 - \eta_m)^2 + (\eta_3 - \eta_m)^2]}, \quad (2)$$

214 where $\eta_m = \frac{\eta_1 + \eta_2 + \eta_3}{3}$, $\eta_1 = \ln(K_1)$, $\eta_2 = \ln(K_2)$, and $\eta_3 = \ln(K_3)$. P_j ranges from 1–2, whereby
215 1 is an isotropic ellipsoid (i.e., a sphere), and $P_j > 1$ indicating the percentage anisotropy, such that
216 $P_j = 1.3$ describes an ellipsoid with 30% anisotropy. The AMS ellipsoid shape is quantified by:

$$T = \frac{2\eta_2 - \eta_1 - \eta_3}{\eta_1 - \eta_3}, \quad (3)$$

217 whereby $T = 1$ describes a uniaxial oblate shape (i.e., planar magnetic fabric) and $T = -1$ describes
218 a uniaxial prolate shape (i.e., linear magnetic fabric). Fabrics presented in this study are classified
219 as weakly (0 – -0.33), moderately (-0.34 – -0.66), and strongly (-0.67 – -1) prolate, or as weakly
220 (0–0.33), moderately (0.34–0.66), and strongly (0.67–1) oblate. The scalar AMS ellipsoid
221 parameters (i.e., K_m , P_j , T) and magnitude and orientation of the principal susceptibilities (K_1 , K_2 ,
222 K_3) were calculated using Anisoft5 (v. 5.1.03; AGICO 2019). The geographically corrected
223 orientations of K_1 , K_2 , and K_3 for each sample location were plotted on equal-area, lower
224 hemisphere stereographic projections (a.k.a. stereonet) and the orientations of the mean principal
225 susceptibilities and their 95% confidence ellipses were calculated using a tensor averaging routine
226 (Jelinek, 1981). Magnetic foliation and lineation measurements are classified as gently (0–30°),
227 moderately (31–60°), and steeply (61–90°) dipping or plunging, respectively. To identify the link
228 between magnetic fabrics and the magma finger geometry, we also quantified the angles between
229 the magma finger long axis measured in the field and both the magnetic foliation strike (α) and the
230 lineation (β), respectively (Fig. 2C).

231 After describing the magnetic fabrics, we characterize the AMS of the samples into two groups of
232 distinct fabrics that either have a gentle to sub-horizontal magnetic foliation (*Fabric Type 1*) or a

233 steep to sub-vertical magnetic foliation (*Fabric Type 2*). *Fabric Type 2* is further subdivided into
234 four groups based on fabric orientation and magnetic ellipsoid shape. We use this classification to
235 discuss a potential link between individual fabrics as well as a potential fabric deformation history
236 during the emplacement of elongate elements.

237 [Insert Figure 3 here.]

238 3.3. *Magnetic mineralogy*

239 During magma flow, crystals can develop a shape-alignment that is parallel to the magma flow
240 direction due to a combination of progressive pure and simple shear, such that the petrofabric
241 foliation and lineation indicate the magma flow plane and axis, respectively (Fig. 2A) (e.g.,
242 Ildefonse et al., 1992; Launeau and Cruden, 1998; Horsman et al., 2005). Crystals may also
243 become imbricated due to high magma velocity gradients that can occur at intrusion margins, such
244 that the closure of the imbricated foliations points in the magma flow direction (Figs. 2A–2B)
245 (e.g., Knight and Walker, 1988; Tauxe et al., 1998; Cañón-Tapia and Chávez-Álvarez, 2004;
246 Poland et al., 2004; Philpotts and Philpotts, 2007). Pure shear flattening due to intrusion inflation
247 and propagation may also result in foliations that parallel the closest host rock contact (Figs. 2A–
248 2B). Importantly, AMS fabrics can be affected by mineralogical controls of the dominating
249 magnetic phases, increasing the complexity to link these fabrics to magma flow processes.

250 The magnetic fabric of ferrimagnetic (s.l.) minerals (e.g., magnetite, maghemite) is influenced by
251 their grain size, shape anisotropy, domain state, and/or grain distribution (Hrouda, 1982; Potter
252 and Stephenson, 1988; Tarling and Hrouda, 1993; Dunlop and Özdemir, 2001; Ferré, 2002).
253 Previous combined petrofabric and magnetic fabric studies have shown that the distribution and
254 shape of magnetite grains are commonly controlled by a framework of the volumetrically dominant

255 silicate mineral phases (e.g., Cruden and Launeau, 1994; Launeau and Cruden, 1998; O’Driscoll
256 et al., 2008). For example, in grains that are large enough to include multiple magnetic domains,
257 referred to as a multi-domain (MD) state, the minimum and maximum magnetic susceptibility
258 coincide with the short- and long-dimension of the grains, respectively, and the magnetic lineation
259 coincides with the SPO (Dunlop and Özdemir, 2001).

260 Although silicate and magnetic fabrics often correlate, there are instances where they differ (e.g.,
261 Launeau and Cruden, 1998; Rochette et al., 1999; Mattsson et al., 2021). For example, where the
262 magnetic fabric is carried by small single-domain (SD) grains, the minimum and maximum
263 magnetic susceptibilities are parallel to the long- and short-dimension of the grain, respectively
264 (Hrouda, 1982; Potter and Stephenson, 1988; Dunlop and Özdemir, 2001; Ferré, 2002). This
265 “inversion” (an inverse fabric) is caused by a higher susceptibility to magnetization along the easy
266 magnetization axis, which is perpendicular to the long-dimension of SD grains (Hrouda, 1982;
267 Potter and Stephenson, 1988; Dunlop and Özdemir, 2001). Magnetic rock fabrics that are purely
268 formed by MD or SD magnetite therefore result in *normal* or *inverse* fabrics, respectively. In such
269 cases, normal fabrics coincide with the magnetite petrofabric, and inverse fabrics form
270 perpendicular to the magnetite petrofabric, where K_1 is perpendicular to the petrofabric foliation
271 and K_3 is parallel to the lineation (Potter and Stephenson, 1988; Rochette and Fillion, 1988;
272 Rochette et al., 1999; Ferré, 2002). Magnetic fabrics that cannot be classified as *normal* or *inverse*
273 are termed *intermediate* and may form when the AMS is carried by a combination of MD and SD
274 magnetite grains (Rochette et al., 1999; Ferré, 2002). Alternatively, where clusters of closely
275 spaced magnetite grains form within a silicate framework, the magnetic responses of multiple
276 grains may magnetically interact (Hargraves et al., 1991; Mattsson et al., 2021). In this case, the
277 shape preferred orientation (SPO) of magnetite plays a secondary role and the AMS is dominated

278 by the grain distribution (distribution anisotropy), which may result in non-coaxial silicate
279 petrofabrics and the magnetic fabrics (Stacey, 1960; Hargraves et al., 1991; Mattsson et al., 2021).

280 The formation of normal, inverse, or intermediate magnetic fabrics and the potential occurrence
281 of a distribution anisotropy make the interpretation of AMS data challenging. It is therefore
282 important to understand the magnetic carriers and their controls on the AMS fabric. To determine
283 the magnetic mineralogy of our samples, we measured the thermomagnetic properties of one
284 specimen from a sample from one of the magma fingers collected in this study, and six specimens
285 from samples collected at sites established through a complete vertical transect in the center of the
286 laccolith (SSL-4). We also obtained isothermal remanent magnetization (IRM) acquisition and
287 backfield isothermal remanent magnetization (BIRM) data on thirteen specimens. Finally, we
288 carried out three-component thermal demagnetization of anhysteretic remanent magnetization
289 (ARM) in a fashion similar to that described by Lowrie (1990) for three component thermal
290 demagnetization of IRM. Measurements were carried out at the M³Ore Lab, University of St.
291 Andrews and in the laboratory at the University of Texas at Dallas. For these analyses, samples
292 that may reflect inverse or intermediate fabrics and samples with a low-to-high bulk susceptibility
293 were selected to get a representative range of mineralogy of the samples studied. The low-to-high
294 temperature, low-field-susceptibility experiments was conducted by measuring the bulk magnetic
295 susceptibility of a powdered rock specimen using a CS4 and CS-L heating and cooling attachment
296 for the KLY-5 Kappabridge. The specimen was first cooled down to -194 °C and the bulk
297 susceptibility was recorded during heating to room temperature and then up to 700 °C, before the
298 temperature was reduced back to room temperature. This procedure provides susceptibility data
299 from a continuous heating-cooling cycle from -194 °C to 700 °C. For specimens collected within
300 the Shonkin Sag laccolith, susceptibility data was collected during a continuous heating-cooling

301 cycle from room temperature to 700 °C. The arising data were collected and used to determine the
302 Verwey transition and the Curie temperature to identify the main ferrimagnetic (s.l.) phase (Dunlop
303 and Özdemir, 2001). Isothermal remanent magnetization acquisition experiments were conducted
304 by using the following procedure: (1) whole core specimens were demagnetized using an LDA5
305 AF Demagnetizer in an alternating maximum field of 200 mT, and a medium decrease rate; (2)
306 the demagnetized specimens were inserted into a MMPM10 pulse magnetizer and exposed to a set
307 field along a single axis direction; (3) the remanence of each sample was then measured in a JR6
308 spinner magnetometer; (4) steps 2 and 3 were repeated as the IRM field was progressively
309 increased from 0.015 T to 1 T. BIRM measurements were subsequently performed by: (1) placing
310 the same specimen upside down in the MMPM10 pulse magnetizer; (2) applying an IRM and then
311 measuring the samples remanence in the JR6 magnetometer; (3) steps 1 and 2 were repeated until
312 the magnetic remanence stopped decreasing and started to increase, usually around 0.1 T.

313 Petrography inspection of thin sections prepared from representative specimens of the magma
314 fingers was evaluated using a polarizing transmitted and reflected light microscope to determine
315 the textural relationship between oxide and silicate mineral phases. Additional μm -scale images
316 of the thin sections were collected with a scanning electron microscope (Quanta 600 MLA),
317 operated with an acceleration voltage of 20 kV, and the chemical composition of these specimens
318 was determined using energy dispersive X-ray analysis.

319

320 3.4. *Quantification of petrofabrics using high-resolution 3-D X-ray computed tomography*

321 The petrofabric of silicate phases (i.e., pyroxene and olivine) in seven selected magma finger
322 specimens was quantified using high-resolution, 3-D X-ray computed tomography (HRXRCT)

323 images. We selected one specimen at each sample location of Finger Hc (Hbc6, Hc7–Hc11) to
324 create a complete HRXRCT dataset for one magma finger, as well as one specimen at JJ-2, which
325 produces tight 95% confidence ellipses and AMS axes orientations that may reflect primary
326 magma flow. HRXRCT data were collected to test if silicate petrofabrics reflect the magnetic
327 fabrics, which aids in identifying the physical significance of the AMS and in better understanding
328 the interplay between AMS and petrofabrics. Samples were scanned using a Zeiss Versa XRM520
329 3-D X-ray microscope at the Australian Resources Research Centre (CSIRO Mineral Resources,
330 Perth, Australia). Scans were conducted using a flat panel detector and an acceleration voltage of
331 120 kV and 10 W. A total of 1,601 projections of the stepwise rotating sample were recorded,
332 which were then merged and stitched to create a 3-D volumetric grid with a voxel size of ~12 μm .
333 We post-processed these grids in Avizo 2020.1 (ThermoFischer) to reduce noise and to separate
334 individual phases, as per Godel (2013). We applied an edge preserving non-local mean filter and
335 manually separated silicate mineral phases from the groundmass based on their grayscale intensity
336 values. Where grayscale intensity values of silicate phases and the groundmass overlap, we
337 calculated variance volumes that were then used to separate the individual mineral phases. Avizo
338 internal functions such as ‘Remove islands’ and ‘Fill holes’ were applied to the separated objects
339 to reduce noise. Both pyroxene and olivine phenocrysts within the shonkinite samples analyzed
340 are ~1–10 mm in size and are clearly visible in hand specimens (Fig. 4A). We therefore classify
341 small, separated objects with a volume $<1 \text{ mm}^3$ as noise and extracted the long, intermediate, and
342 short axis orientations of silicate mineral phases with volumes above this threshold value. The
343 resulting geographic orientations of the mineral phase long and short axes are visualized in equal-
344 area, lower hemisphere stereonet as orientation density distribution contours (modified Kamb
345 method with exponential smoothing (Vollmer, 1995); mplstereonet Python package v.0.6.2). The

346 average SPO is described by a fabric tensor with $V_1 > V_2 > V_3$ representing the long, intermediate,
347 and short axis of the corresponding best fit ellipsoid, respectively, weighted by the axis length
348 (Petri et al., 2020; Mattsson et al., 2021). We analyzed the fabric tensor of each sample using the
349 TomoFab Matlab toolbox (v.1.3) (Petri et al., 2020).

350 We used the same HRXRCT workflow to separate oxide grains within the same specimens. Object
351 volumes $< 10^6 \mu\text{m}^3$ were removed to limit noise effects. To identify a potential influence of the
352 spatial distribution of oxide phases on the magnetic fabric, we calculated the distribution
353 anisotropy (DA) tensor for oxides using the TomoFab Matlab toolbox (v.1.3) as per Mattsson *et*
354 *al.* (2021). The DA tensor is defined by the DA eigenvectors $\lambda_1 > \lambda_2 > \lambda_3$ representing the long,
355 intermediate, and short axis of the DA ellipsoid, respectively. Relatively low values of the
356 corrected degree of anisotropy (P_j) indicate a random grain distribution, whereas relatively high P_j
357 values indicate that grains are spatially distributed along planes ($T > 0$) or lines ($T < 0$) (Mattsson
358 et al., 2021).

359

360 **4. Results**

361 Here we present: (1) petrographic descriptions of shonkinite samples; (2) results of the rock
362 magnetic experiments; and (3) field observations and magnetic- and petro-fabrics measured in
363 samples collected from the main Shonkin Sag laccolith and the four magma fingers. Orientation
364 measurements are given as strike/dip and trend/plunge for planar and linear features, respectively.
365 Average petrofabric and magnetic fabric measurements of sample sites are presented in Table 1
366 and 2, respectively; measurements of individual specimens are presented in the Supplemental
367 Material S2 and S3.

368

369 **4.1. Petrography**

370 The magma fingers are entirely porphyritic shonkinite with a medium-grained groundmass of
371 clinopyroxene, olivine, leucite, minor biotite, and opaque oxides such as magnetite (Fig. 4).
372 Phenocrysts of clinopyroxene, olivine, and leucite are of mm-to-cm size, visible in hand
373 specimens, and float in the groundmass (Figs. 4A–4B). HRXRCT measurements indicate 25–35
374 vol. % of phenocrysts and 65–75 vol. % groundmass (Supplemental Material S4). Up to ~1 cm
375 long, euhedral clinopyroxene phenocrysts have a shape preferred orientation, and locally form star-
376 shaped clusters (Figs. 4A–4D; cf. Hurlbut 1939). Olivine phenocrysts are of mm size, have a
377 euhedral shape, and are occasionally zoned (Fig. 4E). Leucite phenocrysts are euhedral and their
378 diameter ranges from < 1 mm up to ~4 mm (Fig. 4F). Magnetite was identified in both reflected-
379 light and scanning-electron microscopy as the dominant oxide phase (Figs. 4G–4I). Magnetite
380 grains are commonly unaltered and are widely distributed in the shonkinite groundmass, and
381 reflect an interstitial phase (Fig. 4G–4H). Clusters of magnetite were not identified in petrographic
382 analyses, which is supported by a relatively low degree of distribution anisotropy ($P_j = 1.034$ –
383 1.241; Table 1). The petrography of the magma fingers is similar to the main Shonkin Sag laccolith
384 documented in numerous studies (e.g., Pirsson, 1905; Barksdale, 1937; Hurlbut Jr, 1939; Nash and
385 Wilkinson, 1970; Ruggles et al., 2021).

386 [Insert Figure 4 here.]

387 **4.2. Magnetic mineralogy**

388 The results of rock magnetic experiments permit a further determination of the principal magnetic
389 phase that carries the AMS. A low-to-high temperature, low-field-susceptibility experiment
390 determined the Verwey transition and Curie point for sample Hc9 (Fig. 5A). The measurements
391 show a steep initial increase in K_m between -197 °C and the Verwey transition at -165 °C followed
392 by a decrease to 5.6 °C, after which K_m values increase slowly to a well-defined peak at a
393 temperature of about 483 °C, which is followed by a rapid decrease in K_m as temperatures increase
394 to > 600 °C (Fig. 5A). The well-defined Curie point is at about 570 °C (Fig. 5A). During cooling,
395 the K_m measurements show a steep increase between 600 °C and 358 °C followed by a moderate
396 decrease to 48 °C (Fig. 5A). The measurements collected within the Shonkin Sag laccolith (SS-
397 62–SS-66, SS-69) show a well-defined K_m peak at a temperature between ~520–535 °C, followed
398 by a rapid decrease in K_m as temperatures increase to > 600 °C (Fig. 5B). The Curie point occurs
399 at about 580 °C and 605 °C for samples SS-62–SS-66 and SS-69, respectively (Fig. 5B). During
400 cooling, K_m values steeply increase between about 580 °C and 490 °C followed by a gentle increase
401 to ~430 °C and a moderate decrease to ~50 °C (Fig. 5B). A second peak is observed at lower
402 temperatures during both heating (~ 310 °C) and cooling (~370 °C) for SS-69 (Fig. 5B).

403 [Insert Figure 5 here.]

404 IRM and BIRM measurements are useful for characterizing magnetic mineralogy and to estimate
405 magnetic grain size (Dunlop and Özdemir, 2001). IRM experiments show a rapid increase in
406 remanence over a range of low inducing fields and 95% of saturation is achieved by 48 to 78 mT
407 for most of the thirteen specimens analyzed (Fig. 6). The saturation isothermal magnetization
408 (SIRM) for these specimens always is reached below 210 mT with no significant variation
409 observed above this threshold. By extrapolating BIRM curves, we determined the coercivity of
410 remanence (H_{CR}) which ranges from 10 to 15 mT (Fig. 6). Three specimens (Hb1, Hb3, JJ-4) have

411 a higher coercivity. The IRM curves of these specimens rapidly increase within low inducing
412 fields, however, 95% of saturation is reached by 97, 87, and 200 mT, respectively (Figs. 6A, 6C).
413 SIRM occurs below 210 mT for Hb1 and Hb3, and by 1000 mT for JJ-4. H_{CR} measurements based
414 on extrapolated BIRM curves for these samples indicate relatively high coercivity of remanence
415 values of 22 to 29 mT (Fig. 6).

416 [Insert Figure 6 here.]

417 **4.3. AMS and petrofabric analyses**

418 Here we describe: (1) magnetic fabrics of samples collected from the interior of the Shonkin Sag
419 laccolith; and (2) field observations, magnetic fabrics, and petrofabrics of samples collected from
420 magma fingers at the SE laccolith margin. Samples from the main laccolith are presented in merged
421 groups based on their spatial sample location. Magnetic- and petro-fabrics observed within magma
422 fingers are described with respect to the nearest intrusion contact at each individual magma finger.

423 [Insert Table 1 and Table 2 here.]

424 *4.3.1. Shonkin Sag laccolith*

425 Magnetic fabrics were analyzed in four sample groups located to the north-northeast, west,
426 southwest, and south of the geographic center of the Shonkin Sag laccolith (SSL-1, SSL-2, SSL-
427 3, and SSL-4; Fig. 7A). All groups have similar bulk magnetic susceptibilities (K_m) and corrected
428 degree of anisotropy (P_j) values, and their AMS ellipsoids are of similar shape (T) (Table 1). K_m
429 of individual specimens ranges from 0.565×10^{-2} – 11.12×10^{-2} SI, with an average of 3.43×10^{-2}
430 SI (Fig. 7B). The specimens have relatively low P_j values, which increase slightly from 1.0038 to

431 1.0732 with increasing K_m (Fig. 7B). AMS ellipsoids of specimens have moderately prolate to
432 strongly oblate shapes ($T = -0.65$ – -0.97) (Fig. 7C).

433 The magnetic foliation of rocks collected in all sample groups is sub-horizontal and parallel to the
434 inferred upper and lower contacts of the laccolith. Magnetic lineations in SSL-1 are shallow and
435 oriented NE-SW ($229/07^\circ$), and this trend approximately coincides with the overall trend of dykes
436 (069° NE) that crop out NE of the Highwood Mountains (Fig. 7C; indicated by red lines in the
437 stereonets). Magnetic lineations for SSL-2 ($173/04^\circ$) and both SSL-3 ($309/01^\circ$) and SSL-4
438 ($314/02^\circ$) are oriented N-S and NW-SE, respectively, at a high angle ($\sim 75^\circ$) to the aforementioned
439 NE-SW trending dykes (Fig. 7C). We note that the K_1 and K_2 axes of specimens in SSL-1, SSL-2,
440 and, to a minor extent also in SSL-4, are scattered, which causes the 95% confidence ellipses to
441 locally overlap (Fig. 7C). The scattered K_1 axis orientations are grouped in two individual clusters
442 in SSL-2 and SSL-4, trending NNW and WNW, and ENE and NW, respectively (Fig. 7C).

443 [Insert Figure 7 here.]

444 **4.3.2. Magma fingers**

445 For the two individual magma fingers (i.e., Finger II and Finger JJ) and coalesced magma fingers
446 Hb-Hc we describe field observations, AMS data, and, where available, petrographic analysis of
447 fabrics. We describe rock fabrics based on their location with respect to the nearby intrusion
448 contact. Samples are subsequently characterized into two groups of distinct fabrics that either have
449 a gentle to sub-horizontal foliation (*Fabric Type 1*) or a steep to sub-vertical foliation (*Fabric Type*
450 2).

451 Most specimens of the magma fingers have high magnetic K_m values on the order of 10^{-2} SI and
452 only one (JJ-4) out of twenty-one samples has specimens with lower K_m values of $\sim 10^{-4}$ SI (Table
453 2). The corrected degree of anisotropy (P_j) values of individual specimens range from 1.010 to
454 1.030 (Table 2). In most specimens (JJ-2, Hbc6, and Hbc8–Hbc11), the silicate petrofabric
455 foliation is approximately parallel to the corresponding magnetic foliation.

456 4.3.2.1. *Finger II*

457 Finger II is approximately 1.75 m wide and 0.3 m thick, with upper and lower contacts concordant
458 with bedding in the Eagle Sandstone formation ($114/01^\circ$ NE and $121/02^\circ$ NE, respectively; Fig.
459 8A). The lateral tips of Finger II are blunt to rectangular, and the exposed part of the eastern contact
460 is oriented $145/80^\circ$ SW (Fig. 8A). Host rock deformation in the vicinity of the lateral tips cannot
461 be determined due to erosion and scree cover (Fig. 8A). P_j values of samples collected at Finger II
462 range from 1.018–1.030 and K_m varies between 3.03×10^{-2} SI and 4.10×10^{-2} SI (Table 2).

463 Samples located 3–4 cm from the upper and lower intrusion contact are characterized by a steep
464 to moderate magnetic foliation (II-2 = $175/74^\circ$ W; II-4 = $163/49^\circ$ ENE), a gently to moderately
465 NNW plunging magnetic lineation (II-2 = $342/39^\circ$; II-4 = $350/09^\circ$), and a weakly to moderately
466 prolate fabric shape ($T = -0.49$ – -0.31) (Fig. 8, Table 2). At these locations, the magnetic foliations
467 form a moderate to steep angle of 47.5 – 74.5° to the nearby sub-horizontal host rock contacts, and
468 strike at an α angle of up to 30° to the magma finger long axis, which trends 145° SE (Figs. 8B).
469 In contrast to samples near the upper and lower finger contacts, measured magnetic foliations
470 located 2–6 cm from the lateral finger tips (II-1 = $145/89^\circ$ NE; II-5 = $153/60^\circ$ SW) strike at an α
471 angle of 0 – 8° to the magma finger long axis and are thus sub-parallel to the intrusion contact (Fig.
472 8B). Samples II-1 and II-5 are characterized by a steeply and gently plunging magnetic lineation

473 (II-1 = 142/72°; II-5 = 316/28°), and a moderately oblate ($T = 0.35$) and weakly prolate ($T = -0.16$)
474 fabric shape, respectively. In the intrusion core (i.e., II-3), approximately 15–16 cm to the upper
475 and lower intrusion contacts and 37 cm to the eastward lateral finger tip, the magnetic foliation
476 (022/84° E) is steeply dipping and strikes at an α angle of 57° to the magma finger long axis. The
477 mean K_I orientation of II-3 is steep (157/81°), orthogonal to the upper and lower contacts, and the
478 fabric shape is weakly oblate ($T=0.20$).

479 [Insert Figure 8 here.]

480

481 4.3.2.2. *Finger JJ*

482 Finger JJ is approximately 2.1 m wide and 0.45 m thick and has strata-concordant flat top and
483 bottom contacts (138/03° NE and 126/02° NE, respectively; Fig. 9A). The lateral tips of Finger JJ
484 are asymmetric, being pointed to the SW and blunt on the NE where it is oriented 135/80° NE (Fig.
485 9A). Host rock bedding at the lateral tips of Finger JJ is deflected upwards (Fig. 9A). P_j values of
486 samples collected at Finger JJ range from 1.011–1.027 and K_m varies between 0.04×10^{-2} SI and
487 4.30×10^{-2} SI with K_m at JJ-4 being two orders of magnitude smaller than the remaining samples
488 (Table 2).

489 The magnetic foliations of samples located 3–6 cm from the upper and lower intrusion contact (JJ-
490 2 = 086/04° N; JJ-4 = 086/05° S) are sub-parallel to the nearby intrusion contact (138/03° NE,
491 126/02° NE), and the shallow plunging K_I (327/03°, 117/03°) trends approximately parallel to the
492 magma finger long axis (135° SE). In both JJ-2 and JJ-4, the mean principal susceptibility
493 directions are well-defined and have tight 95% confidence ellipses (Fig. 9B). The fabric shape at

494 JJ-2 is weakly prolate ($T = -0.06$), whereas JJ-4 has a moderately oblate shape ($T = 0.39$). In
495 contrast, sample JJ-5 is located ~9 cm from the NE lateral finger tip and is characterized by a steep
496 magnetic foliation ($131/83^\circ$ SW), which is sub-parallel to the intrusion contact ($135/80^\circ$ NE). The
497 magnetic lineation at JJ-5 is steeply plunging ($248/83^\circ$) and the fabric shape is weakly oblate ($T =$
498 0.13). Individual specimen K_1 , K_2 , and K_3 directions in sample JJ-5 are slightly dispersed but 95%
499 confidence ellipses are tight (Fig. 9B). Samples JJ-1 and JJ-3 are located 18–27 cm from the upper
500 and lower intrusion contacts and are considered to represent the intrusion core. JJ-1 is located ~31
501 cm from the SW lateral finger tip and has a steep magnetic foliation ($030/75^\circ$ SE) that strikes sub-
502 perpendicular to the magma finger long dimension (135° SE) (Fig. 9B). The mean K_1 axis is gently
503 plunging SW ($207/12^\circ$) and the fabric shape is weakly prolate ($T = -0.11$). In contrast to JJ-1, JJ-3
504 is characterized by a steep magnetic foliation ($135/73^\circ$ NE) and a gently plunging lineation
505 ($133/05^\circ$) that strikes and plunges sub-parallel to the magma finger long dimension, respectively
506 (Fig. 9B). The fabric shape at JJ-3 is weakly prolate ($T = -0.21$).

507 Petrofabric analyses of silicate phases at JJ-2 indicate a sub-horizontal foliation ($026/06^\circ$ SE) sub-
508 parallel to the nearby host rock contact, which coincides with the magnetic foliation. In contrast to
509 the SE trending mean K_1 axis ($327/03^\circ$), V_1 gently plunges ENE ($073/04^\circ$) at an angle of 62° to the
510 magma finger long dimension (Fig. 9C; Table 1). The petrofabric shape is moderately oblate ($T =$
511 0.38), which contrasts with the weakly prolate magnetic counterpart (Tables 1–2).

512 [Insert Figure 9 here.]

513

514 4.3.2.3. *Coalesced Fingers Hb-Hc*

515 Coalesced magma fingers Hb and Hc are approximately 6.7 m and 1.9 m wide, 1.2 m and at least
516 0.7 m thick, respectively, with sub-horizontal, strata-concordant upper and lower contacts (104/02°
517 NNE, 079/01° NNW, 108/02° NNE; Fig. 10A). The NE lateral tip of Finger Hc has a blunt to
518 rectangular geometry and forms a steeply dipping (118/72° SW) crosscutting contact with the host
519 rock (Fig. 10A). Host rock deformation at the lateral tip remains undefined due to erosion. The
520 upper contacts of Fingers Hb and Hc are vertically offset with Finger Hb being ~0.65 m higher
521 than the top contact of Hc. A ~0.75 m wide and ~0.4 m thick, NE-dipping step connects Fingers
522 Hb and Hc, and it has a gently dipping (143/18° NE), strata-discordant upper contact with host
523 rock bedding (Fig. 10A). P_j values of samples collected at Fingers Hb and Hc range from 1.010–
524 1.025 and K_m varies between 2.10×10^{-2} SI and 3.87×10^{-2} SI (Table 2).

525 Three samples are located close to the upper or lower intrusion contacts (Hb1=15 cm, Hb3=20 cm,
526 Hc7=8 cm). Hb1 and Hb3 are characterized by gently inclined magnetic foliations, which are at
527 an angle of 30° and 27° with the respective nearby contact, and by gently plunging lineations (Hb1
528 = 050/20°; Hb3 = 251/18°) (Fig. 10B). The magnetic foliations of the weakly oblate Hb1 (013/30°
529 ESE; $T = 0.08$) and the moderately prolate Hb3 (117/25° SW; $T = -0.41$) dip toward and away
530 from the adjacent intrusive step to the east, respectively (Fig. 10B). The NE-SW trend of K_l in
531 both Hb1 (050/20°) and Hb3 (251/18°) points toward the adjacent WNW-ESE striking intrusive
532 step with a high β angle of 47–68° to the magma finger long axis (118° SE) (Fig. 10B, Table 2). In
533 contrast to Hb1 and Hb3, Hc7 has a moderately dipping magnetic foliation (145/63° SW) at an
534 angle of ~63° to the nearby contact. The magnetic lineation (211/60°) plunges SW and the fabric
535 shape at Hc7 is moderately oblate ($T=0.44$).

536 Samples Hbc5 and Hbc6 are located 13 cm and 20 cm from the upper intrusion contact, within the
537 intrusive step that connects the fingers Hb and Hc, and they have weakly prolate ($T=-0.15$) and

538 moderately oblate ($T=0.41$) fabric shapes, respectively (Fig. 10A). At both locations, the magnetic
539 foliation is moderately and steeply dipping ($Hbc5 = 031/58^\circ$ SE, $Hbc6 = 082/71^\circ$ S) and K_I axes
540 orientations are moderately and steeply plunging south ($Hbc5 = 162/51^\circ$, $Hbc6 = 194/70^\circ$). The
541 magnetic foliation at Hbc5 forms an angle of 53° to the nearby host rock contact; contact
542 orientation measurements above Hbc6 cannot be determined due to limited 3D exposure (Fig.
543 10A).

544 Sample Hc8 was collected 17 cm from the lateral SW finger tip of Hc and has a weakly oblate
545 fabric shape ($T=0.03$) (Fig. 10A). Hc8 is characterized by a steeply dipping magnetic foliation
546 ($030/84^\circ$ SE) at an angle of 86° to the nearby contact ($118/72^\circ$ SW), and a steeply plunging K_I axes
547 orientations ($194/70^\circ$) (Fig. 10A–B).

548 Samples Hb2, Hb4, and Hc9–Hc11 are located in the core of the intrusions with distances of ~30–
549 50 cm to the closest upper or lower intrusion contact (Fig. 10A) and are characterized by a steep
550 to sub-vertical magnetic foliation. Except for Hb4, magnetic foliations within the intrusion core
551 are striking SW ($Hb2 = 143/73^\circ$ NE, $Hc9 = 128/80^\circ$ NE, $Hc10 = 157/79^\circ$ NE, $Hc11 = 116/87^\circ$ NE)
552 with alpha angles of 2 – 39° to the finger long axis orientation (Fig. 10B). K_I axis orientations at
553 Hb2 are moderately plunging SE ($129/37^\circ$), whereas at Hc9–Hc11, K_I axes are steep to sub-vertical
554 ($Hc9 = 019/79^\circ$, $Hc10 = 013/71^\circ$, $Hc11 = 345/86^\circ$; Table 2). The ellipsoid shape of the described
555 fabrics ranges from weakly to moderately prolate at Hb2, Hc10, and Hc11, and is weakly oblate
556 at Hc9 (Table 2). The magnetic foliation ($034/86^\circ$ NE) and lineation ($261/85^\circ$) at Hb4 dip and
557 plunge sub-vertical, and they are both oriented sub-perpendicular to the magma finger long
558 dimension (118°) (Fig. 10B). The fabric shape at Hb4 is weakly oblate ($T=0.05$).

559 [Insert Figure 10 here.]

560

561 Petrofabric analyses of the main silicate phases (i.e., pyroxene and olivine) at Hbc6 and Hc7–Hc11
562 indicate a moderately to strongly oblate fabric shape ($T = 0.38\text{--}0.78$) except for Hc11, which is
563 weakly prolate ($T = -0.10$). The petrofabric foliation at Hbc6, Hc8, Hc9, and Hc11 approximately
564 reproduces the magnetic foliation, with angles between both foliation planes ranging from 11° to
565 34° (Fig. 11A–B). Except for Hc8 where foliations are oriented approximately perpendicular to
566 the magma finger long dimension (118°), petrofabric and magnetic foliations at Hbc6, Hc9, and
567 Hc11 strike SE, approximately in the magma finger long dimension. At Hc10, both petrofabric
568 and magnetic foliations dip NE. However, the gently dipping petrofabric foliation ($127/32^\circ$ NE)
569 contrasts with the steep magnetic foliation ($157/79^\circ$ NE), which form at an angle of 52° (Fig. 11B).
570 A comparable deviation in foliation orientations is observed at Hc7 (Fig. 11B). Here, the
571 petrofabric foliation is shallowly dipping north ($084/22^\circ$ N), whereas the magnetic foliation is
572 moderately dipping SW ($145/63^\circ$ SW), resulting in an angle of 75° between both foliation planes.
573 In all analyzed specimens, the mean V_I axes orientations are sub-horizontal to gently plunging,
574 which contrasts with the steep to sub-vertical K_I axes orientations (Fig. 11B).

575 [Insert Figure 11 here.]

576

577 **4.3.3. Characterization of fabric types**

578 Four samples collected in the magma fingers (JJ-2, JJ-4, Hb1, Hb3) and all four sample groups
579 collected within the main laccolith (SSL-1 – SSL-4) are characterized by sub-horizontal to gently
580 inclined magnetic foliations and lineations, which we refer to as *Fabric Type 1*. Within the magma

581 fingers, *Fabric Type 1* is only observed in samples collected within 3–19 cm of the upper and
582 lower margins of Fingers JJ and Hb (Figs. 9, 10; Table 2). We note that although samples <8 cm
583 from the upper and lower margins were collected from Finger II (II-2, II-4) and Hc (Hc-7), they
584 do not display the characteristics of *Fabric Type 1* (Figs. 8 and 10).

585 In contrast to the sub-horizontal *Fabric Type 1*, *Fabric Type 2* is characterized by moderate to sub-
586 vertical magnetic foliations, which are further subdivided into four distinct groups based on their
587 orientation and shape. Five samples (II-2, II-4, II-5, JJ-3, Hb2) are characterized by a steep to
588 moderate magnetic foliation approximately striking parallel to the magma finger long dimension,
589 a gently to moderately plunging magnetic lineation, and a weakly to moderately prolate fabric
590 shape ($T = -0.49 - -0.16$), which we refer to as *Fabric Type 2A* (Figs. 8–10; Table 2). Similar to
591 *Fabric Type 2A*, the magnetic foliation of *Fabric Type 2B* (II-1, JJ-5, Hbc6, Hc7, Hc9) strikes
592 approximately parallel to the magma finger long dimension. The magnetic lineations, however,
593 are steep to sub-vertical and fabric shapes are weakly to moderately oblate ($T = 0.13-0.44$). Two
594 samples (Hc10, Hc11) have a steep to sub-vertical magnetic foliation and lineation and weakly
595 prolate shapes ($T = -0.31 - -0.25$), which we characterize as *Fabric Type 2C* (Figs. 10B–10C). The
596 magnetic foliation at these locations strikes oblique to sub-parallel to the magma finger long
597 dimension ($\alpha = 2^{\circ}-39^{\circ}$). *Fabric Type 2D* is characterized by a moderately inclined (Hbc5) and
598 steep to sub-vertical (II-3, JJ-1, Hb4, Hc8) magnetic foliations that strike sub-perpendicular to the
599 magma finger long axis (Figs. 8B, 9B, 10B). The magnetic lineation at these locations plunges
600 steeply (II-3, Hb4, Hc8), moderately (Hbc5), and gently (JJ-1) and the fabric shape ranges from
601 weakly prolate to weakly oblate ($T = -0.15 - 0.20$).

602

603 **5. Discussion**

604 *5.1. Characterization of the magnetic mineralogy and the significance of AMS*

605 *5.1.1. Magnetic mineralogy*

606 Based on rock magnetic experiments and petrographic observations, Ruggles et al. (2021)
607 suggested that both magnetite and titanomagnetite with a pseudo-single domain (PSD) state and
608 multidomain (MD) state are the dominant magnetic phases in the rocks exposed at the margin of
609 the Shonkin Sag laccolith and its peripheral sills. Our observations support the dominance of
610 titanomagnetite as the magnetic carrier within the magma fingers based on: (1) a relatively high
611 K_m of $> \sim 10^2$ SI (Tarling and Hrouda, 1993); (2) rapidly increasing K_m followed by a slightly
612 temperature dependent flat plateau in low-temperature regimes between -197 – 5 °C (Fig. 5A)
613 (Dunlop and Özdemir, 2001); and (3) a Curie point estimate of 570 °C (Fig. 5A) (Dunlop and
614 Özdemir, 2001). The Curie Point of pure magnetite occurs at 580 °C; however, this temperature
615 decreases for titanomagnetite with increasing Ti content (Akimoto, 1962). The Curie point
616 estimate of 570 °C suggests that titanomagnetite with a low Ti content of ~ 1 – 2 % is the dominant
617 ferrimagnetic phase in the samples studied (Akimoto, 1962).

618 IRM and BIRM measurements also indicate that the AMS of all samples is dominated by a
619 relatively low coercivity phase such as titanomagnetite. IRM curves and the magnetic field
620 strength required to completely saturate a sample (SIRM) can be used to estimate the magnetic
621 grain size (cf. Dunlop and Özdemir, 2001). MD magnetite will completely saturate by ~ 80 – 200
622 mT, fine grained SD magnetite will completely saturate by ~ 300 mT, and SIRM values just above
623 ~ 200 mT indicate the presence of PSD grains (Dunlop and Özdemir, 2001). The relatively low
624 SIRM of < 210 mT for twelve out of thirteen samples indicate a PSD to MD state (Fig. 6) (Dunlop

625 and Özdemir, 2001). IRM and BIRM measurements combined with low-to-high temperature
626 susceptibility data suggest that PSD to MD titanomagnetite are the dominant phases responsible
627 for the AMS in the marginal sills and comprising magma fingers, and by comparison to related
628 studies, the main Shonkin Sag laccolith (Ruggles et al., 2021). Samples with higher coercivities
629 (Hb1, Hb3, JJ-4) are located near the upper or lower margin of magma fingers (Fig. 6). We suggest
630 that weathering or alteration caused by interaction between the intruding magma and the pore
631 water-saturated host rock may have altered titanomagnetite to relatively high coercivity minerals
632 close to the host rock contact (Dunlop and Özdemir, 2001). Potential effects of these high
633 coercivity minerals on the AMS fabrics have been considered during fabric interpretation.

634

635 5.1.2. *Origin of the magnetic fabrics*

636 Before interpreting primary magma flow and magma emplacement mechanisms from AMS data,
637 it is important to first consider whether the magnetic fabrics measured have been affected and/or
638 altered by other processes. Ruggles et al. (2021) found that MD and PSD magnetite are the
639 dominant magnetic phases in shonkinite rocks at the margin of the laccolith, and where the rocks
640 are undeformed and fresh they considered magnetic fabrics in their samples to be normal primary
641 magma flow fabrics. However, a range of processes can modify and should be considered when
642 interpreting magnetic fabrics. For example, magnetic foliation planes and/or magnetic lineations
643 at a high-angle to the plane of a magma finger (i.e., *Fabric Type 2D*) (Figs. 8B, 9B, and 10B) may
644 possibly be interpreted as intermediate or inverse fabrics due to the presence of SD magnetite
645 (Potter and Stephenson, 1988; Rochette and Fillion, 1988; Rochette et al., 1999). We can discount
646 *Fabric Type 2D* being related to the presence of SD magnetite populations as our IRM analyses

647 indicate no detectable SD magnetite, so we consider that sub-vertical magnetic lineations and
648 foliations that strike sub-perpendicular to the magma finger long axis are unlikely to be caused by
649 mineralogical effects. Alternatively, when magnetite grains are closely spaced or occur in clusters,
650 adjacent grains can interact magnetically to alter magnetic fabrics (Hargraves et al., 1991;
651 Mattsson et al., 2021). Because our petrographic analyses found no magnetite clusters, together
652 with the generally low degree of distribution anisotropy (Table 1), distribution anisotropy of
653 magnetite probably can be ruled out as contributing to the AMS of our samples.

654 Syn- and post-emplacement tectonic deformation can modify or completely overprint magma
655 emplacement-related magnetic fabrics, which can add further complexity to the interpretation of
656 AMS data. However, the Highwood Mountains of Montana are tectonically undeformed (e.g.,
657 Pollard et al., 1975), making it an ideal location to study magma emplacement processes and flow
658 kinematics within intrusions. During tectonic overprinting, uniform fabrics representing the strain
659 associated with tectonism should affect all sample locations (e.g., Burton-Johnson et al., 2019).
660 Although uniform sub-horizontal magnetic foliations have been documented within the main
661 Shonkin Sag laccolith (Fig. 7C), considerable variations in magnetic fabrics within the marginal
662 magma fingers (Figs. 8B, 9B, 10B) are interpreted to indicate that no tectonic overprinting
663 occurred. Alternatively, magnetic fabrics can be inversed when they align with cooling joints
664 oriented orthogonal to the intrusion margin (Trippanera et al., 2020). In this scenario, K_1 axes will
665 be oriented parallel to the fracture trend orthogonal to the intrusion margin due to potential
666 secondary magma migration during relatively slow intrusion cooling (Trippanera et al., 2020).
667 However, magma fingers located at the SE margin of the Shonkin Sag laccolith do not show
668 significant evidence of cooling joints, and fabric orientations of samples collected near minor
669 fractures (e.g., II-2–II-4) are not parallel to the fracture plane, suggesting that fabrics were not

670 affected by fractures. Relatively rapid cooling rates should characterize the magma fingers due to
671 their small size (0.3–1.2 m thick; 1.75–6.7 m wide), suggesting that convective magma flow is
672 unlikely to have occurred within them (e.g., Gibb and Henderson, 1992; Holness et al., 2017). The
673 lack of evidence for post-emplacement overprinting, cooling joints, or convective flow, together
674 with the coincidence between the magnetic foliation strike and lineation trend with magma finger
675 long axes in many samples (Figs. 8B, 9B, and 10B), suggest that the AMS data from our samples
676 can be interpreted to reflect primary syn-emplacement processes such as magma flow and/or
677 intrusion inflation.

678

679 5.2. *Shonkin Sag laccolith emplacement*

680 Samples from sites established in all four arbitrary areas of the Shonkin Sag laccolith (SSL-1, SSL-
681 2, SSL-3, SSL-4) yield a sub-horizontal magnetic foliation and a predominantly oblate fabric
682 shape, regardless of their location (Fig. 7). These observations are consistent with measurements
683 at the laccolith margin in areas of no to little deformation and/or alteration (Ruggles et al., 2021).
684 The shape and orientation of magnetic fabrics observed across the Shonkin Sag laccolith may
685 reflect sub-horizontal magma flow and/or vertical shortening, likely related to initial emplacement
686 processes and, possibly, the subsequent inflation and/or deflation of the laccolith soon after
687 emplacement. In primary magma flow within sheet-like intrusions, we expect the magnetic
688 foliation to form parallel to the magma flow plane and K_I principal axes will be aligned in the flow
689 direction (Figs. 2A–2B) (e.g., Knight and Walker, 1988). The alignment of K_I occurs due to
690 progressive simple shear flow and results in monoclinic fabrics with plane strain ellipsoids ($T \approx 1$)
691 (e.g., Cruden and Launeau, 1994; Ferré et al., 2002; Poland et al., 2004; Horsman et al., 2005).

692 Alternatively, during vertical inflation of igneous sheet intrusions due to the continued throughput
693 of magma, magnetic fabrics will record vertical shortening caused by pure shear flattening strain,
694 which results in biaxial, oblate fabrics ($T \approx 0$) (Fig. 2B) (e.g., Roni et al., 2014). During inflation
695 the fabric shape at the intrusion margin will become progressively more oblate and the foliation
696 will align with the orientation of the closest host rock contact (e.g., Roni et al., 2014).

697 [Insert Figure 12 here.]

698 We interpret sub-horizontal, oblate magnetic fabrics within the main Shonkin Sag laccolith to
699 record a combination of sub-horizontal magma flow and vertical intrusion inflation. Assuming that
700 K_I indicates the primary magma flow direction, we suggest that the AMS within the laccolith
701 indicates: (1) NE-SW oriented magma flow NNE of the intrusion center (SSL-1; $K_I = 229/07^\circ$);
702 (2) NNW-SSE oriented magma flow W of the intrusion center (SSL-2; $K_I = 173/04^\circ$); and (3) NW-
703 SE oriented magma flow SW and S of the intrusion center (SSL-3 and SSL-4; $K_I = 309/01^\circ$ and
704 $314/02^\circ$, respectively) (Fig. 12). We note that samples across the main laccolith were collected
705 from varying elevation levels (Supplemental Material S1), such that they may reflect fabrics within
706 multiple magma pulses, which may explain both the slightly dispersed K_I axis orientations and the
707 formation of two K_I axis clusters in sample groups SSL-2 and SSL-4 (Fig. 7C). The strongly oblate
708 fabric shape across all four sample groups may reflect flattening of the fabrics against the roof,
709 which is consistent with a conceptual model suggested by Morgan (2018), who applied Pascal's
710 principle to explain laccolith emplacement. We interpret the maintenance of preferred K_I axis
711 orientations in sample groups SSL1–SSL4 to reflect primary magma flow during horizontal
712 laccolith growth. Based on the data available, the relative timing of K_I axis alignment in magma
713 flow direction cannot be determined such that the alignment may have occurred both before and/or
714 after laccolith inflation and resulting horizontal overburden uplift.

715 Feeders of sills and laccoliths are commonly described to be either linear, such as dykes and
716 inclined sheets, or point-like conduits, from which magma flows linearly or radially, respectively
717 (e.g., Cruden et al., 1999; Ferré et al., 2002; Galerne et al., 2011). If the Shonkin Sag laccolith was
718 fed via a point source, we would expect the feeder to be located approximately in the intrusion
719 center, which would be the origin of a radial magma flow pattern. However, this scenario is not
720 supported by the NNW-SSE to NW-SE trending magnetic lineation at sample groups SSL-2, SSL-
721 3, and SSL-4 (Fig. 12). We suggest that the Shonkin Sag laccolith was fed via a NE-SW striking
722 dyke that terminated in the NE quadrant of the laccolith, close to sample group SSL-1 (Fig. 12).
723 NW-SE directed flow of magma sub-perpendicular to the strike of the feeder is consistent with K_1
724 orientations in sample groups SSL-2, SSL-3, SSL-4 (Figs. 7C, 12). The NE-SW trending K_1
725 direction in sample group SSL-1 is sub-parallel to the strike of the potential feeder-dyke. We
726 therefore hypothesize that the dyke terminated S to SW of sample group SSL-1, which may have
727 resulted in a fanning magma flow pattern near the dyke tip (Fig. 12).

728 Although Pollard et al. (1975) assumed radial magma flow from the laccolith center to explain the
729 NW-SE trend of magma fingers at the SE laccolith margin, similar magma finger trends are also
730 consistent with magma being supplied via a NE-SW striking dyke (Fig. 12). In this scenario, linear
731 magma flow sub-perpendicular to the feeder dyke coincides with the long-dimension of magma
732 fingers (Fig. 12). Numerous NE-SW striking dykes are located SW of the laccolith, and they are
733 part of the radial dyke swarm that surrounds the main volcanic complex of the Highwood
734 Mountains (Figs. 3B–3C). These observations suggest NE directed magma transport from the main
735 volcanic complex toward the Shonkin Sag laccolith, which supports our proposed feeder model.
736 Additional magnetic fabric analyses of samples from the eastern part of the laccolith could help to
737 test the proposed model and to better constrain both the feeder type and location.

738

739 5.3. *Tying magnetic fabrics to magma finger emplacement and growth*

740 Given we have determined that the magnetic fabrics likely record magma emplacement processes,
741 we hypothesize there are two competing mechanisms, namely primary magma flow and intrusion
742 inflation (Fig. 2b), that control the shape and orientation of fabrics in pipe-like intrusions. For
743 example, assuming primary magma flow along a horizontal magma finger, we expect crystals to
744 align with the magma velocity profile, resulting in horizontal foliations close to the upper and
745 lower contact and steep foliations near the lateral magma finger tips (e.g., Merle, 2000) (Figs. 2B,
746 13A). In both cases, the foliation parallels the nearest intrusion contact and K_1 aligns in magma
747 finger long dimension, which we interpret to reflect the primary magma flow direction. Imbricated
748 foliations may occur at distance to the upper and lower magma finger contacts due to the magma
749 velocity gradient (e.g., Knight and Walker, 1988) (Figs. 2A–2B). During magma finger
750 emplacement, magma fingers both increase in width and vertically inflate (e.g., Galland et al.,
751 2019). This magma finger inflation causes pure shear flattening strain which may modify the
752 initial, flow-related fabrics (e.g., Merle, 2000). For example, in case of vertical intrusion inflation,
753 we expect foliations near the upper and lower intrusion margin to parallel the nearest contact with
754 K_1 remaining aligned in finger long dimension, whereas at lateral finger tips, fabrics may become
755 stretched along the intrusion contact, resulting in steep K_1 axes (Fig. 13A). During magma finger
756 widening, we expect fabrics at the lateral magma finger tips to flatten against the nearest intrusion
757 contact, likely resulting in steep foliations and lineations (Fig. 13A). Primary magma flow and
758 intrusion inflation can occur simultaneously, producing a hybrid fabric that may be dominated by
759 one process or another. Importantly, AMS data reflect magnetic fabrics at the time of local magma
760 solidification such that individual samples collected across the magma fingers may reflect different

761 emplacement stages (e.g., Philpotts and Philpotts, 2007). Spatially variable magma flow may
762 therefore result in adjacent fabrics that are not directly related (Fig. 13A).

763 Below, we use magnetic fabric data, petrofabric analyses and field observations to interpret the
764 emplacement of magma fingers located at the margin of the Shonkin Sag laccolith. Critically, we
765 interpret the primary magma finger flow direction to parallel the SE trend of the magma fingers,
766 which point away from their feeding sills and the main Shonkin Sag laccolith (Pollard et al., 1975).
767 This allows us to focus on interpreting internal 3-D flow within the elongate magma fingers, to tie
768 magnetic fabrics to intrusion emplacement and growth, and test our hypothesis of competing
769 emplacement mechanisms (i.e., primary magma flow and intrusion inflation) as outlined above.

770

771 [Insert Figure 13 here.]

772 5.3.1. *Fabric Type 1 – Primary magma flow and vertical intrusion inflation*

773 *Fabric Type 1* is comparable to fabrics observed within the Shonkin Sag laccolith (Fig. 7C). As
774 within the Shonkin Sag laccolith, we interpret *Fabric Type 1* to have formed during sub-horizontal
775 magma flow and/or vertical shortening (Figs. 13A–13B). Because vertical magma finger inflation
776 commonly occurs simultaneously with horizontal magma flow, we consider it likely that *Fabric*
777 *Type 1*, as observed in upper and lower magma finger margins (JJ-2, JJ-4, Hb1, Hb3), represents
778 a hybrid of both processes, where the relative effect of each process may vary between locations
779 (Fig. 13B). For example, the sub-horizontal foliation in samples JJ-2 and JJ-4 is sub-parallel to the
780 closest upper or lower intrusion-host rock contact and K_1 trends sub-parallel to the finger long axis
781 (Fig. 9B). In combination with the weakly prolate to moderately oblate fabric shape, these

782 orientations suggest that progressive simple shear during magma flow may be the dominant
783 process recorded by the AMS, superimposed by pure shear flattening due to minor vertical
784 shortening (Fig. 13B). Considering the sample locations and assuming that magma solidification
785 occurs first at the intrusion margins, we interpret the magnetic fabrics in samples JJ-2 and JJ-4
786 represent primary magma flow during a relatively early emplacement stage (Figs. 13A–13B).

787 A similar interpretation may account for the magnetic fabrics in samples Hb1 and Hb3 that are
788 located close to the upper and lower margins of Finger Hb (Fig. 10A). In contrast to the sub-
789 horizontal foliation in samples JJ-2 and JJ-4, the magnetic foliation in samples Hb1 and Hb3 dip
790 gently in the direction of the magma finger long axis or away from the intrusive step that connects
791 Fingers Hb and Hc (Fig. 10). These gently dipping foliations in rocks located close to the sub-
792 horizontal intrusion-host rock contact, combined with their weakly oblate to moderately prolate
793 AMS ellipsoids may indicate a relatively low degree of vertical flattening. We could also interpret
794 the gently dipping foliations to be imbricated fabrics, whereby sample Hb1 records primary
795 magma flow towards the SE and sample Hb3 indicates a foliation inclined toward either the former
796 lateral tip of Finger Hb or to the intrusive step that connects Fingers Hb and Hc, potentially
797 indicating crossflow between Hb and Hc (Figs. 10, 13A) (e.g., Magee et al., 2016b). Given the
798 weakly oblate to moderately prolate AMS ellipsoids in these samples, we interpret K_1 to be a
799 primary magma flow indicator. Therefore, their NE-SW trending K_1 directions may indicate flow
800 oblique ($\beta = 47^\circ\text{--}68^\circ$) to the finger long axis, possibly related to local flow of magma between
801 Fingers Hb and Hc after they had coalesced (Fig. 13A), or magma flow toward a solidified step.
802 Because primary magma flow within sheet intrusions is commonly described to form oblate fabrics
803 parallel to the flow plane with K_1 aligned in flow direction, similar to *Fabric 1*, we propose that
804 *Fabric 1* could be the starting point for fabrics classified as *Fabric 2*, which we interpret below

805 (Figs. 13B–13C). We note that fabrics close to the lateral magma finger tips may start as steep
806 foliations instead of a *Fabric 1* due to combined simple and pure shear flow close to the steep
807 intrusion contact (Figs. 13A–13B).

808

809 5.3.2. *Fabric Type 2A, 2B – Horizontal shortening caused by intrusion widening*

810 We interpret the moderate to steep magnetic foliations to represent magma emplacement processes
811 because they strike slightly oblique to the magma finger long axis ($\alpha = 0\text{--}30^\circ$) and the magnetic
812 lineation is gently to moderately plunging and broadly parallels the magma finger axis (Table 2).
813 These fabrics are observed near to upper and lower intrusion contacts (II-2, II-4), at lateral finger
814 tips (II-5), and along the centerline of magma fingers (JJ-3, Hb2). *Type 2A* fabrics may result from
815 the superimposition of a sub-horizontal, oblate *Type 1* fabric, by a sub-horizontal NE-SW
816 shortening strain, approximately perpendicular to the magma finger long dimension (Figs. 13B–
817 13C). Previous field studies have shown that space for magma fingers can be partly accommodated
818 by host rock shortening when magma pushes against the host rock ahead of both the frontal and
819 lateral intrusion tips (e.g., Pollard et al., 1975; Wilson et al., 2016; Spacapan et al., 2017; Galland
820 et al., 2019). This process may result in compaction, folding, and shear failure of host rock layers
821 and is commonly associated with blunt to rectangular intrusion tips as is observed in Fingers II
822 and Hc (Figs. 8A, 10A) (Wilson et al., 2016; Spacapan et al., 2017; Galland et al., 2019; Stephens
823 et al., 2021; Walker et al., 2021). We suggest that when magma fingers widen, magma or magma
824 mush near the host rock walls gets squeezed, resulting in horizontal fabric shortening sub-
825 perpendicular to the lateral margins and in vertical fabric stretching, which is reflected in the
826 development of a new or overprinting fabric (i.e., *Fabric Type 2B*; Figs. 13B–13C). Similar

827 modification of fabrics with an inflating finger could occur to those located adjacent to an internal
828 steeply inclined transient boundary, such as an inwardly migrating crystallization front (Fig. 13A).
829 Regardless, this NE-SW shortening causes pure shear flattening of fabrics against lateral intrusion-
830 host rock contacts or internal boundaries (II-5), resulting in steep foliations sub-parallel to the host
831 rock contact (Figs. 13B–13C). We also hypothesize that the strength of fabric overprinting decays
832 with distance from the lateral tip or internal boundary, which may for example be reflected by the
833 more prolate AMS ellipsoid of II-2, II-4, JJ-3, and Hb2 compared to sample II-5 (Fig. 13B).

834 The magnetic foliation in *Fabric Type 2B* is slightly oblique to the magma finger long axis ($\alpha =$
835 $0\text{--}36^\circ$) and the samples that exhibit this fabric type are located close to (II-1, JJ-5) and farther away
836 from (Hbc6, Hc7, Hc9) lateral finger tips, which suggests that they may record similar magma
837 emplacement processes as described for *Fabric Type 2A* (i.e., horizontal NE-SW intrusion
838 inflation). However, in contrast to *Fabric Type 2A* where K_1 plunges gently to moderately along
839 the magma finger, K_1 of *Fabric Type 2B* is steeply inclined (Figs. 13B–13C; Table 2). As in *Fabric*
840 *Type 2A*, horizontal intrusion inflation may have led to NE-SW pure shear flattening as well as
841 fabric stretching at lateral intrusion tips, which resulted in the formation of *Type 2B* fabrics (Figs.
842 13B–13C). The weakly to moderately oblate AMS ellipsoids suggest a higher degree of NE-SW
843 pure shear flattening compared to *Fabric Type 2A* (Fig. 13C). *Fabric Type 2B* may therefore reflect
844 a more advanced stage of magma finger widening compared to *Fabric Type 2A*. The *Type 2B*
845 fabric in sample Hbc6 is associated with the step that connects Fingers Hb and Hc. Here, the
846 magnetic foliation strikes E-W, which indicates potential local crossflow of magma between the
847 coalesced magma fingers (Fig. 13A).

848

849 5.3.3. *Fabric Type 2C, 2D – Horizontal shortening caused by intrusion lengthening*

850 Similar AMS ellipsoid axes orientations in both *Type 2B* and *2C* fabrics suggest a formation of
851 *Fabric Type 2C* due to the sequence of magma emplacement processes as described above (cf.
852 *Fabric Type 2A* and *2B*) (Figs. 13B–13C). However, in contrast to the weakly to moderately oblate
853 *Type 2B* fabrics, the AMS ellipsoid of *Fabric Type 2C* is weakly to moderately prolate with a steep
854 to sub-vertical K_1 direction (Figs. 10, 13C). Assuming that *Fabric Type 2C* formed by progressive
855 deformation of *Fabric Type 2B*, two scenarios may be considered: (1) vertical stretching during
856 NE-SW magma finger widening (Figs. 13A–13B); or (2) horizontal NW-SE shortening at an
857 arrested frontal finger tip due to continued magma supply (Figs. 13B–13C). When magma fingers
858 widen and magma pushes against the host rock or against a transient solidification boundary (cf.
859 *Fabric 2A, 2B*), vertical flow along the boundary may result in stretching fabrics (Figs. 13A–13B).
860 Field observations of clinopyroxene crystals oriented sub-parallel to the intrusion-host rock contact
861 at lateral finger tips are consistent with this hypothesis (Fig. 2D). However, the effect of vertical
862 stretching in samples Hc10 and Hc11 should be minor because they are located approximately in
863 the core of Finger Hc. This is also reflected in the silicate mineral lineation, which plunges gently
864 in the finger long axis direction, contrasting with the sub-vertical magnetic fabrics (Fig. 11B).
865 Alternatively, sub-horizontal shortening parallel to the NW-SE finger long axis may have
866 overprinted a sub-vertical, NW-SE striking, weakly to moderately oblate *Fabric Type 2B* foliation,
867 resulting in steep, weakly prolate magnetic fabrics (Hc10, Hc11; Figs. 13B–13C). As noted above,
868 NW-SE shortening is likely to occur at frontal magma finger tips (e.g., Cruden and Launeau, 1994;
869 Magee et al., 2016b) and may also occur away from an arrested intrusion tip if magma supply
870 continues (Figs. 13B–13C) (Cruden and Launeau, 1994).

871 With increasing horizontal shortening and pure shear flattening strain parallel to the magma finger
872 long axis, *Type 2C* fabrics may evolve into steep to sub-vertical (II-3, JJ-1, Hb4, Hc8), or
873 moderately inclined (Hbc5), weakly prolate to weakly oblate fabrics, which strike sub-
874 perpendicular to the finger long axis (i.e., *Fabric Type 2D*; Figs. 13B–13C). Alternatively, a sub-
875 vertical foliation may form due to free grain rotation of minerals, which then get trapped with their
876 long and intermediate SPO axes perpendicular to the flow direction (e.g., Cañón-Tapia and
877 Chávez-Álvarez, 2004). If this rotation occurs within a crystallizing, horizontally flowing magma,
878 the growing framework of silicate phases may prevent further rotation of grains toward the magma
879 flow plane, resulting in sub-vertical magnetic fabrics (Launeau and Cruden, 1998). However, free
880 grain rotation in a simple shear magma flow occurs periodically and is therefore not predictable
881 (Launeau and Cruden, 1998). We thus consider it unlikely that *Fabric Type 2D* in the core of both
882 discrete and coalesced magma fingers (II-3, JJ-1, Hb4, Hc8) reflects a similar timestep in the grain
883 rotation cycle.

884 Sub-vertical magnetic foliations that are perpendicular to the magma finger long axis have been
885 also observed in a previous study of a sill in the Karoo Igneous Province that is composed of
886 multiple elongate elements (Hoyer and Watkeys, 2017). Hoyer and Watkeys (2017) interpreted
887 these fabrics to reflect magma flow between coalesced elements, perpendicular to the intrusion
888 long dimension. However, because *Type 2D* fabrics are also observed within discrete magma
889 fingers (II-3, JJ-1) and due to the similarity in sample locations, we hypothesize that horizontal
890 shortening parallel to the magma finger long axis due to the final intrusion tip arrest may have
891 caused the formation of *Fabric Type 2D* (Figs. 13B–13C). Critically, the magma rheology has to
892 enable viscous flow such that grains can rotate and overprint previously formed fabrics (e.g.,
893 Launeau and Cruden, 1998; Cañón-Tapia and Chávez-Álvarez, 2004). Crystallization and local

894 solidification may therefore limit fabric overprinting to areas of localized magma flow. This could
895 explain the occurrence of *Type 2C* and *2D* fabrics in the intrusion core and along the center line,
896 which are plausible locations for localized magma flow during a late stage of magma emplacement
897 (Figs. 13A–13B).

898 The moderately SE dipping foliation in sample Hbc5 is located close to the upper contact of the
899 step that connects Fingers Hb and Hc (Fig. 10A). Here the magnetic foliation dips toward the
900 frontal finger tip and may indicate imbrication of grains against the intrusion roof (e.g., Knight
901 and Walker, 1988; Philpotts and Philpotts, 2007). In this case, Hbc5 records primary magma flow
902 and the magnetic lineation oriented obliquely to the magma finger long axis may indicate local
903 crossflow of magma between Fingers Hb and Hc (Fig. 13A).

904

905 *5.3.4. Comparison of magnetic- and silicate petro-fabrics*

906 The magnetic and silicate mineral foliations in samples Hbc6, Hc8, Hc9, Hc10, and Hc11 are
907 broadly coincident (Fig. 11B). However, the maximum SPO direction of the silicate phases (V_1)
908 plunges gently (2–28°) in these samples, which contrasts with the steep to sub-vertical orientation
909 of K_1 (Fig. 11B; Tables 1 and 2). Angles between K_1 and V_1 axis orientations range from 44°
910 (Hbc6) up to 75–88° (Hc7–Hc11). These differences may be caused by the presence of multiple
911 silicate mineral sub-fabrics, which are averaged in the fabric tensor. For example, the orientation
912 density distribution plots of samples Hc8 and Hc9 show girdles of long axes orientations with two
913 distinct clusters (Fig. 11A). These clusters may reflect individual sub-fabrics and thus influence
914 the average V_1 and V_2 fabric tensor orientations.

915 An alternative explanation for the different K_I and V_I orientations is the so-called “logjam” effect
916 (Launeau and Cruden, 1998). This occurs when crystallizing silicate phases form a mineral
917 framework in which individual grains start to interact during magma flow, preventing large grains
918 from rotating and locking up or jamming the silicate petrofabric (Launeau and Cruden, 1998). At
919 this stage, only smaller grains such as magnetite are able to rotate in response to continuing flow
920 of the magma mush, although their degree of rotation will be limited by adjacent silicate grains
921 (Launeau and Cruden, 1998). A relatively high degree of crystallization and a low volume
922 percentage of melt (between ~30 and 50 %) are required to cause grain interaction and limit the
923 rotation of silicate phases (Launeau and Cruden, 1998). Although the moderate modal
924 concentration of silicate phenocrysts (~25–35 vol.%; Supplemental Material S4; Nash and
925 Wilkinson, 1970) in our samples indicates a melt volume percentage of greater than 65 %, we
926 suggest that the logjam model may explain some of the variations between magnetic and silicate
927 petrofabrics, if the fabric overprinting occurred during a late stage of emplacement when the
928 groundmass started to crystallize.

929 If the amount of late stage crystallization was high enough to cause interaction between individual
930 grains, the logjam model may explain the ~74° discrepancy between K_I and V_I in sample JJ-2 (Fig.
931 9D). Sample JJ-2 is located close to the upper margin of Finger JJ, where both the magnetic and
932 silicate petrofabric foliations are sub-parallel to the host rock contact (Fig. 9D). We therefore
933 interpret the foliations in sample JJ-2 to reflect the primary magma flow plane (e.g., Féménias et
934 al., 2004). Given that the overall SE magma flow direction is constrained from field observations
935 (Pollard et al., 1975), we interpret the NW-SE orientation of K_I as primary flow indicator. The
936 ~62° difference between V_I and the finger long axis may indicate: (1) oblique flow of magma
937 toward the lateral finger tip, which is suggested above to occur during intrusion widening (Figs.

938 2D, 13B); or (2) a stable orientation of silicate phases in a plane of constant magma velocity with
939 V_1 oblique to the magma flow direction (e.g., Jeffery, 1922). We suggest that increased
940 crystallization at the intrusion margins locked up the silicate petrofabrics that reflects either
941 intrusion widening or stable grain orientations oblique to the magma flow, whereas magnetite
942 grains remained mobile and re-aligned according to potential changes in magma flow kinematics.

943 The discrepancy between magnetic- and petro-fabric lineations could also be explained by
944 intermediate magnetic fabrics, where K_2 and K_3 axis orientations are swapped (Rochette et al.,
945 1999; Ferré, 2002). One indicator for potential intermediate magnetic fabrics are the coaxial fabric
946 orientations, where K_2 equals V_3 and vice versa (JJ-2, Hc8–Hc11; Figs. 9D and 11B). If we assume
947 intermediate magnetic fabrics at JJ-2 and Hc8–Hc11, the “corrected” magnetic fabrics would
948 coincide with the petro-fabrics such that K_1 at Hc9–Hc11 would change toward a sub-horizontal
949 lineation that trends approximately in magma finger long dimension, resulting in *Type 2A* fabrics
950 potentially indicating an interplay of magma flow along a steep boundary and horizontal finger
951 widening (Figs. 13A–13B). The “corrected” K_1 axis orientations at JJ-2 and Hc8 are sub-horizontal
952 and trend approximately perpendicular to the magma finger long dimension, potentially reflecting
953 an emplacement stage of magma finger widening. At Hc8, the sub-vertical magnetic foliation
954 remains perpendicular to the magma finger long dimension which may still reflect NW-SE
955 shortening (cf. Section 5.3.3). Although intermediate and/or inverse magnetic fabrics cannot be
956 ruled out completely, our analyses suggest that the presented AMS data likely reflect normal
957 fabrics (cf. Section 5.1). We further note that V_1 axis orientations are scattered and form girdle
958 structures and multiple clusters in the orientation density distribution; these clusters potentially
959 reflect individual sub-fabrics, such that the mean V_1 axis orientation may not be reliable.

960

961 5.4. *The complexity of magma flow in finger-like intrusions*

962 When magma flows in relatively thin sheets (<5 m), the resulting magnetic fabrics are more
963 uniform than in thicker sheets, which can be due to: (1) magnetic fabrics in a larger part of the
964 chilled margin in thinner sheets may record primary magma flow (e.g., Philpotts and Philpotts,
965 2007; Magee et al., 2016b); (2) thicker sheets have the potential to undergo thermal convection,
966 which will overprint emplacement-related laminar flow fabrics (e.g., Holness et al., 2017); and (3)
967 thicker sheets may comprise multiple magma pulses, with each pulse having its own magnetic
968 fabric characteristics (e.g., Magee et al., 2016b). Although the magma fingers described here are
969 relatively thin (~0.3–1.2 m), their magnetic fabrics show a range of fairly defined patterns and are
970 not uniform (Fig. 13B). If magma flow in elongate elements is comparable to laminar fluid flow
971 in a pipe, velocity profiles are expected to be axisymmetric with shapes that will vary depending
972 on the fluid rheology (e.g., Pinho and Whitelaw, 1990). In such cases, imbricate fabrics are
973 expected to form along the intrusion margin. However, cyclic particle rotation, a stable orientation
974 of particles in a plane of constant magma velocity, or consecutive flow processes (i.e., primary
975 magma flow and horizontal/vertical intrusion inflation) can overprint fabrics caused by laminar
976 flow and may explain irregular fabrics in elements (e.g., Jeffery, 1922; Cañón-Tapia and Chávez-
977 Álvarez, 2004). Due to the five distinct fabric patterns which are observed in similar sample
978 locations in both individual and coalesced magma fingers, we consider it unlikely that these fabrics
979 represent a similar stage of cyclic particle rotation. Instead, the distinct patterns in magnetic fabrics
980 observed in the magma fingers suggest that: (1) magma flow in elongate elements is more complex
981 than in planar sheet intrusions; and (2) magnetic fabrics record other syn-emplacement processes
982 such as intrusion inflation rather than primary magma flow as discussed above (Fig. 13).

983 Syn-emplacement deformation of magnetic fabrics has been described in high-viscosity magmas,
984 such as the Sandfell laccolith, Iceland (Mattsson et al., 2018). Here, magnetic fabrics were affected
985 by S-C fabrics which formed in response to compression perpendicular to the intrusion contact
986 and shearing during intrusion inflation; the magnetic foliation parallels the S-plane (i.e., foliation)
987 whereas flow bands are parallel to C-planes (i.e., shear plane) (Mattsson et al., 2018). In a different
988 scenario, magnetic fabrics within the felsic Cerro Bayo cryptodome, Argentina, deformed in
989 response to multiple magma pulses, where intruding magma folded magma of previous pulses
990 (Burchardt et al., 2019). These observations highlight an interplay between magnetic fabric
991 orientation and syn-emplacement deformation. Importantly, this deformation is observed in felsic
992 intrusions and fabric overprinting is controlled by high magma viscosities which enable the
993 formation of syn-emplacement S-C structures or folding of previous magma pulses (REFS). These
994 observations contrast with deformation of fabrics in low-viscosity intrusions, which we assign to
995 an interplay of primary magma flow and both horizontal and vertical inflation, as described in this
996 contribution. Dynamically changing flow regimes within elongate magma fingers may cause
997 multifold overprinting of primary flow fabrics resulting in complex and potentially diverging
998 magnetic- and petro-fabrics.

999

1000 5.5. *Is flow in coalesced magma fingers sheet-like or localized?*

1001 Our data suggest that distinct emplacement processes operated during the intrusion of the Shonkin
1002 Sag magma fingers, associated with varying flow kinematics within coalesced magma fingers.
1003 These findings highlight the importance of sample locations and densities when interpreting
1004 magnetic- and petro-fabrics, especially within elongate elements and/or sheet intrusions

1005 comprising coalesced elements. We compared the fabric types observed in discrete (II and JJ) and
1006 coalesced (Hb and Hc) magma fingers and found that they reflect similar magma emplacement
1007 processes such as along-finger primary magma flow and both horizontal and/or vertical inflation.
1008 However, magnetic fabrics oriented oblique to the long axis of magma fingers Hb and Hc (Hb1,
1009 Hb3, Hbc5, Hbc6) suggest more complex and locally varying magma flow where magma fingers
1010 coalesce (Fig. 10B). Such complex flow patterns may result from: (1) oblique flow between
1011 adjacent magma fingers (Fig. 13A) (Hoyer and Watkeys, 2017; Martin et al., 2019); (2) locally
1012 turbulent flow due to the intrusion and connector geometry (Andersson et al., 2016); (3) flow
1013 localization due to closure of a connector caused by increased crystallinity (Holness and
1014 Humphreys, 2003; Magee et al., 2016b) (Fig. 13A); or (4) varying magma rheology, temperature,
1015 or velocity between the adjacent magma fingers (Magee et al., 2013, 2016b). Based on the data
1016 presented here, both sheet-like and localized magma flow in coalesced magma fingers is likely to
1017 have occurred. However, although samples within (Hbc5, Hbc6) and in the vicinity (Hb1, Hb3) to
1018 the step between Fingers Hb and Hc may be affected by local oblique magma flow between fingers,
1019 most of the fabrics observed in coalesced fingers are comparable to those in discrete examples.
1020 This suggests that along-magma finger flow and intrusion inflation within a coalesced finger
1021 remained considerably isolated and may imply a potential localized flow regime (Fig. 13A).

1022 Identifying areas of sheet-like or localized magma flow within coalesced elements has implications
1023 for the emplacement of, and related magma flow pathways within sheet intrusions, which
1024 contributes to knowledge on sheet intrusion architecture and trans-crustal magma plumbing
1025 systems. These findings can be applied to the exploration of economic sulfide (Ni-Cu-Co-PGE)
1026 ore deposits, which are often linked to areas of both localized magma flow and high magma flux
1027 (e.g., Barnes et al., 2016). Localized, high magma flux can cause mechanical erosion and

1028 subsequent incorporation of the surrounding host rock into the magma, and as such, this process
1029 can contribute to accommodating the intruding magma and to increasing the crustal sulfur content
1030 (e.g., Gauert et al., 1996; Barnes et al., 2016). Understanding if and where in sheet intrusions
1031 magma flow may localize can therefore help to improve strategies for Ni-Cu-Co-PGE exploration.

1032 On a crustal-scale, identifying flow kinematics within both individual and coalesced elements
1033 contributes to unravelling magma transport within large magma plumbing systems. For example,
1034 inclined to sub-vertical elements can act as feeders within interconnected sill networks,
1035 contributing to vertical magma transport (Guo et al., 2013; Magee et al., 2014). At shallow levels,
1036 this localized magma flow within elements and sheet intrusions may further result in horizontally
1037 distributed fissure eruptions at the Earth's surface. Understanding where in sheet intrusions magma
1038 flow can localize therefore is important for characterizing the architecture of and the internal
1039 magma transport within both individual and interconnected sheet intrusions.

1040

1041 **6. Conclusions**

1042 We analyzed the AMS in four sample groups from the Shonkin Sag laccolith (Highwood
1043 Mountains, Montana, USA) and from samples from two isolated and two coalesced magma fingers
1044 that emerge from the laccolith's SE margin. The results suggest that the Shonkin Sag laccolith was
1045 fed by a NE-SW striking dyke, which is part of the swarm that radiates from the Highwood
1046 Mountains. The SE trending magma fingers at the SE margin of the laccolith are close to
1047 perpendicular to the inferred feeder-dyke. The AMS of samples from the magma fingers indicate
1048 magnetic fabrics that vary over short distances (i.e., less than 20 cm) that we interpret to reflect:
1049 (1) primary magma flow, which is mainly recorded in the upper and lower intrusion margins; and

1050 (2) syn-magmatic emplacement processes such as horizontal and/or vertical intrusion inflation,
1051 which is mainly observed at the lateral tips and cores of the fingers. We classified five distinct
1052 fabric patterns, which we ascribe to fabric overprinting during different stages of magma finger
1053 emplacement, namely along-finger primary magma flow and intrusion inflation. Silicate
1054 petrofabric foliations obtained from high-resolution 3-D X-ray computed tomography data are
1055 similar to the magnetic fabrics determined for the magma fingers. Differences between magnetic
1056 fabric and petrofabric long axis orientations may result from increased crystallization, which
1057 results in grain interaction and jams up individual grains of the silicate framework, whereas small
1058 magnetite grains remain mobile and re-align according to magma emplacement processes. Within
1059 the connector between two coalesced magma fingers, magnetic lineation and foliation are oblique
1060 to the finger long axis, which suggests potential local crossflow between magma fingers once they
1061 are coalesced. Despite this local crossflow between coalesced fingers, magnetic fabrics suggest
1062 that magma flow may localize in each particular coalesced finger. The range of rock fabrics
1063 obtained from the magma fingers highlights the importance of sample locations when using AMS
1064 data to interpret primary magma flow. This is particularly important for elongate elements and
1065 sheet intrusions that comprise amalgamated elements, and has important implications for
1066 understanding their internal flow kinematics. The occurrence of distinct fabric types and fabric
1067 overprinting within a small area of a magma finger, as discussed in this contribution, may also
1068 imply that uniform data from larger sheet intrusions only reflect part of the intrusion emplacement
1069 history. This raises the question regarding at what point during intrusion emplacement the more
1070 complex fabric pattern are overprinted and become erased from the strain record? Our magnetic-
1071 and petro-fabric data reveal the interplay between competing forces during magma emplacement
1072 (i.e., along-finger flow and finger inflation), and imply processes that have been previously

- 1073 unrecognized. These magma emplacement processes and the overprinting of earlier magma flow
- 1074 kinematics should be considered when interpreting data from large-scale sheet intrusions.

1075

1076 **Supplemental Material**

1077 Supplemental Material are available on the figshare repository,
1078 <https://doi.org/10.26180/17108447.v1> (“Supplemental Material 2.1.1 and 3”).

1079 S0: 3D drone imagery of the studied outcrop

1080 S1: Table with coordinates of sample locations

1081 S2: Table with AMS measurements of all individual specimens

1082 S3: Table with SPO measurements of all individual grains

1083 S4: Volume measurements of individual phases based on HRXRCT scans

1084 S5: Raw BSE images of magnetite grain shown in Figure 4 I

1085

1086 **Acknowledgments**

1087 We are grateful to the landowners Robert W. Ebeling, Holly Ebeling, and Jo Alice Juedeman for
1088 permitting access to the stunning cliff faces of the Shonkin Sag laccolith. We thank David Lageson
1089 for providing the portable drill used to collect rock samples. All drill holes in magma fingers
1090 produced during this study were subsequently infilled following the code of conduct for rock
1091 coring. We are grateful to Belinda Godel and Anja Slim for help with processing and analyzing
1092 HRXRCT data, Barbara Etschman for SEM analyses, and Uchitha Nissanka Arachchige for field
1093 assistance. We gratefully acknowledge helpful reviews by Steffi Burchardt and Sven Morgan, and
1094 we thank Ian Alsop for his editorial handling of the manuscript. JK acknowledges a Monash
1095 Graduate Scholarship and a Graduate Research Completion Award. ARC and CM acknowledge
1096 support from ARC Discovery Grant DP 190102422.

1097

1098

1099 **References cited**

1100 Automatic citation updates are disabled. To see the bibliography, click Refresh in the Zotero tab.

1101

1102

1103 **Figure captions:**

1104 Figure 1: (A) Coalesced, elongate elements highlighted in 3-D seismic reflection data of a sill
1105 located offshore NW Australia (Köpping et al., 2022). Thickness map shows distinct thickness
1106 variations between adjacent elements. (B) Discrete magma fingers at the SE margin of the Shonkin
1107 Sag laccolith, Montana, USA (Pollard et al., 1975). (C) Coalesced magma fingers form a
1108 continuous sheet intrusion at the SE margin of the Shonkin Sag laccolith, Montana, USA (Pollard
1109 et al., 1975).

1110 Figure 2: (A) Schematic diagram illustrates magma flow within igneous intrusions and highlights
1111 potential flow fabrics (modified after Magee et al., 2016). (B) Schematic diagrams illustrate
1112 expected fabrics resulted from primary magma flow and both vertical and horizontal magma finger
1113 inflation. (C) Schematic diagram shows the angular relation between both the foliation and
1114 lineation and the trend of magma fingers; α defines the angle between the foliation strike and the
1115 magma finger trend, and β defines the angle between the lineation and the magma finger trend.
1116 (D) Field photograph of a lateral magma finger tip located at the SE margin of the Shonkin Sag
1117 laccolith (Montana, USA). Black lines indicate the maximum shape preferred orientation of
1118 clinopyroxene phenocrysts and show the alignment of minerals sub-parallel to the intrusion-host
1119 rock contact.

1120 Figure 3: Location maps of study area. (A) Overview map shows the location of the Highwood
1121 Mountains, Montana, USA. (B) Simplified geological map indicates sedimentary, volcanic, and
1122 igneous rocks of the Highwood Mountains (based on the Geological Map of the quadrangles ‘Fort
1123 Benton’ and ‘Belt’; 1:100,000 scale; available from the Montana Bureau of Mines and Geology
1124 (2021)). Field examples of magma fingers are shown in Figures 1B and 1C. (C) Rose diagram
1125 shows the trend of dykes that crop out NE of the Highwood Mountains (color-coded in red in
1126 Figure 3B). (D) Schematic diagram of a cliff face located at the southeast Shonkin Sag laccolith
1127 margin shows the transition of the laccolith into 5 emerging sills. Sills No. 3 and No. 5 show
1128 evidence of both coalesced and discrete magma fingers. Note that magma fingers indicated in the
1129 cross section are schematic and do not represent the accurate size or location. Sample locations
1130 and drone imagery of the outcrop are provided in Supplemental Material S0–S1. The cross section
1131 location is indicated in Figure 3B.

1132 Figure 4: (A) Field photograph and (B) HRXRCT scan of shonkinite from magma fingers at the
1133 SE Shonkin Sag laccolith margin. Note the shape preferred orientation of Cpx. Cpx–
1134 clinopyroxene; Lct–leucite. (C–H) Photomicrographs of shonkinite under (C–E) crossed-polarized
1135 light, (F) plane-polarized light, and (G, H) reflected light. Ol–olivine; Bt–biotite; Mag–magnetite.
1136 (I) Backscattered electron image of a magnetite grain. Note that two images with different
1137 brightness-level were merged to visualize the internal magnetite structure and the groundmass.
1138 Raw-images are shown in the Supplemental Material S5.

1139 Figure 5: Low-to-high temperature, low-field susceptibility experiment of (A) a sample collected
1140 within magma finger Hc (Hc9) and (B) samples collected along a vertical transect through the
1141 Shonkin Sag laccolith (SSL-4). Arrows in (A) indicate the Verwey transition ($-165\text{ }^{\circ}\text{C}$), blocking
1142 temperature ($483\text{ }^{\circ}\text{C}$), and the Curie point ($570\text{ }^{\circ}\text{C}$). Gray lines in (A) show data from samples
1143 collected from the Shonkin Sag laccolith and emerging sills as presented by Ruggles et al. (2021).
1144 Continuous and dashed lines indicate heating and cooling curves, respectively. (B) Specimens of
1145 sample group SSL-4 have blocking temperatures at about $520\text{--}530\text{ }^{\circ}\text{C}$ and Curie points occur
1146 between $580\text{--}605\text{ }^{\circ}\text{C}$.

1147 Figure 6: Results of isothermal remanent magnetization (IRM) and back-field IRM (BIRM)
1148 demagnetization experiments for samples in (A) fingers Hb and Hc, (B) finger II, and (C) finger
1149 JJ. Black dashed lines in BIRM plots are extrapolated BIRM curves which are used to estimate the
1150 coercivity of remanence (H_{CR}). Schematic diagrams of magma fingers indicate the sample location
1151 (white dots).

1152 Figure 7: (A) Satellite image (GoogleEarth) of the Shonkin Sag laccolith shows the sample
1153 locations of sample group SSL-1–SSL-4 (white dots) and the location of magma fingers at the SE
1154 laccolith margin; laccolith outline after Hurlbut Jr. (1939). (B) Plot of the mean magnetic
1155 susceptibility (K_m) against the corrected degree of anisotropy (P_j) for all specimens. (C) Equal-
1156 area lower hemisphere stereonet plots of the anisotropy of magnetic susceptibility (AMS) for the
1157 four sample groups. 95% confidence ellipses are plotted for the average principal susceptibility
1158 axes. Orientation density distribution contours are visualized for K_I axes. Red lines indicate the
1159 average trend (069° NE) of dykes NE of the Highwood Mountains, as is shown in Fig. 3C. P_j is
1160 plotted against the shape parameter (T) for each sample group.

1161 Figure 8: (A) Photomosaic and interpreted sketch for magma finger II. Dots are color-coded for
1162 the fabric type and highlight the individual sample locations, and structural measurements
1163 (strike/dip) indicate the intrusion-host rock contact. (B) Equal-area, lower hemisphere stereonet
1164 plots of the anisotropy of magnetic susceptibility (AMS) for the five sample locations (II-1–II-5)
1165 shown in (A). 95% confidence ellipses are plotted for the average principal susceptibility axes.
1166 The magma finger trend (145° SE; gray arrow) is inferred from the intrusion-host rock contact at
1167 the lateral E finger tip (145/80° SW). (C) Plots for the corrected degree of anisotropy (P_j) against
1168 both the mean magnetic susceptibility (K_m) and the shape factor (T). Note that the plotted
1169 measurements are mean values for each sample location in finger II. (D) Schematic diagram shows
1170 the magnetic fabric orientation at the approximate sample location within magma finger II.

1171 Figure 9: (A) Photograph and interpreted sketch for magma finger JJ. Dots are color-coded for the
1172 fabric type and highlight the individual sample locations, and structural measurements (strike/dip)
1173 indicate the intrusion-host rock contact. (B) Equal-area, lower hemisphere stereonet plots of the
1174 anisotropy of magnetic susceptibility (AMS) for the five sample locations (JJ-1–JJ-5) shown in
1175 (A). 95% confidence ellipses are plotted for the average principal susceptibility axes. The magma
1176 finger trend (135° SE; gray arrow) is inferred from the intrusion-host rock contact at the lateral NE
1177 finger tip (135/80° NE). (C) Equal-area, lower hemisphere stereonet plots show the orientation
1178 density distribution of long axes (V_1) and short axes (V_3) orientations of clinopyroxene and olivine
1179 crystals in JJ-2; average fabric tensor axes orientations (V_1 , V_2 , V_3) are indicated. (D) Equal-area,
1180 lower hemisphere stereonet plot shows the comparison of AMS (K_1 , K_2 , K_3) and fabric tensor (V_1 ,
1181 V_2 , V_3) axes orientations. (E) Plots for the corrected degree of anisotropy (P_j) against both the mean
1182 magnetic susceptibility (K_m) and the shape factor (T). Note that the plotted measurements are mean
1183 values for each sample location in finger JJ. (F) Schematic diagram shows the magnetic fabric
1184 orientation at the approximate sample location within magma finger JJ.

1185 Figure 10: (A) Photomosaic and interpreted sketch for magma fingers Hb and Hc. Dots are color-
1186 coded for the fabric type and highlight the individual sample locations, and structural
1187 measurements (strike/dip) indicate the intrusion-host rock contact. (B) Equal-area, lower
1188 hemisphere stereonet plots of the anisotropy of magnetic susceptibility (AMS) for the eleven
1189 sample locations (Hb1–Hc11) shown in (A). 95% confidence ellipses are plotted for the average
1190 principal susceptibility axes. The magma finger trend (118° SE; gray arrow) is inferred from the

1191 intrusion-host rock contact at the lateral NE finger tip of Hc (118/72° SW). (C) Plots for the
1192 corrected degree of anisotropy (P_j) against both the mean magnetic susceptibility (K_m) and the
1193 shape factor (T). Note that the plotted measurements are mean values for each sample location in
1194 fingers Hb and Hc. (D) Schematic diagram shows the magnetic fabric orientation at the
1195 approximate sample location within the coalesced magma fingers Hb and Hc.

1196 Figure 11: (A) Equal-area, lower hemisphere stereonet plots show the orientation density
1197 distribution of long axes (V_1) and short axes (V_3) orientations of clinopyroxene and olivine crystals
1198 for one sample in the intrusive step (Hbc6) and for finger Hc (Hc7–Hc11); average petrofabric
1199 tensor axes orientations (V_1 , V_2 , V_3) are indicated. (B) Equal-area, lower hemisphere stereonet plots
1200 show the comparison of AMS (K_1 , K_2 , K_3) and petrofabric tensor (V_1 , V_2 , V_3) axes orientations.

1201 Figure 12: Simplified geological map of the Shonkin Sag laccolith shows the potential feeder-dyke
1202 location, magnetic lineation orientations, and inferred magma flow pathways. The plunge of
1203 magnetic lineations is indicated at the tip of solid black arrows. The geological map is based on
1204 the quadrangle ‘Fort Benton’ (1:100,000 scale) available from the Montana Bureau of Mines and
1205 Geology (2021); laccolith outline after Hurlbut Jr. (1939).

1206 Figure 13: (A) Schematic cross-section diagrams show a time series of magma finger emplacement;
1207 cross sections are oriented perpendicular to both the magma finger long axis and the primary
1208 magma flow direction. Magma flow and emplacement processes and the expected associated
1209 fabrics are indicated. Note that changing magma flow dynamics and local magma solidification
1210 can result in adjacent fabrics that are not directly related (iv). (B) Schematic 3-D diagram shows
1211 all fabric types as observed in the magma fingers studied, their spatial occurrence, and how they
1212 may develop over time. Magma flow processes such as primary flow, inflation, and fabric
1213 stretching/flattening are indicated. (C) Schematic Flinn diagram shows interpreted strain paths and
1214 fabric overprinting due to primary magma flow and both horizontal and vertical inflation.

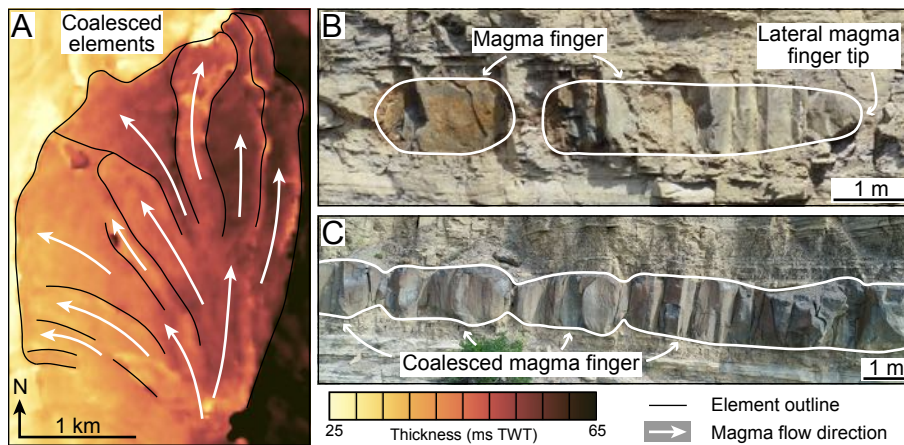


Figure 1: (A) Coalesced, elongate elements highlighted in 3-D seismic reflection data of a sill located offshore NW Australia (Köpping et al., 2022). Thickness map shows distinct thickness variations between adjacent elements. (B) Discrete magma fingers at the SE margin of the Shonkin Sag laccolith, Montana, USA (Pollard et al., 1975). (C) Coalesced magma fingers form a continuous sheet intrusion at the SE margin of the Shonkin Sag laccolith, Montana, USA (Pollard et al., 1975).

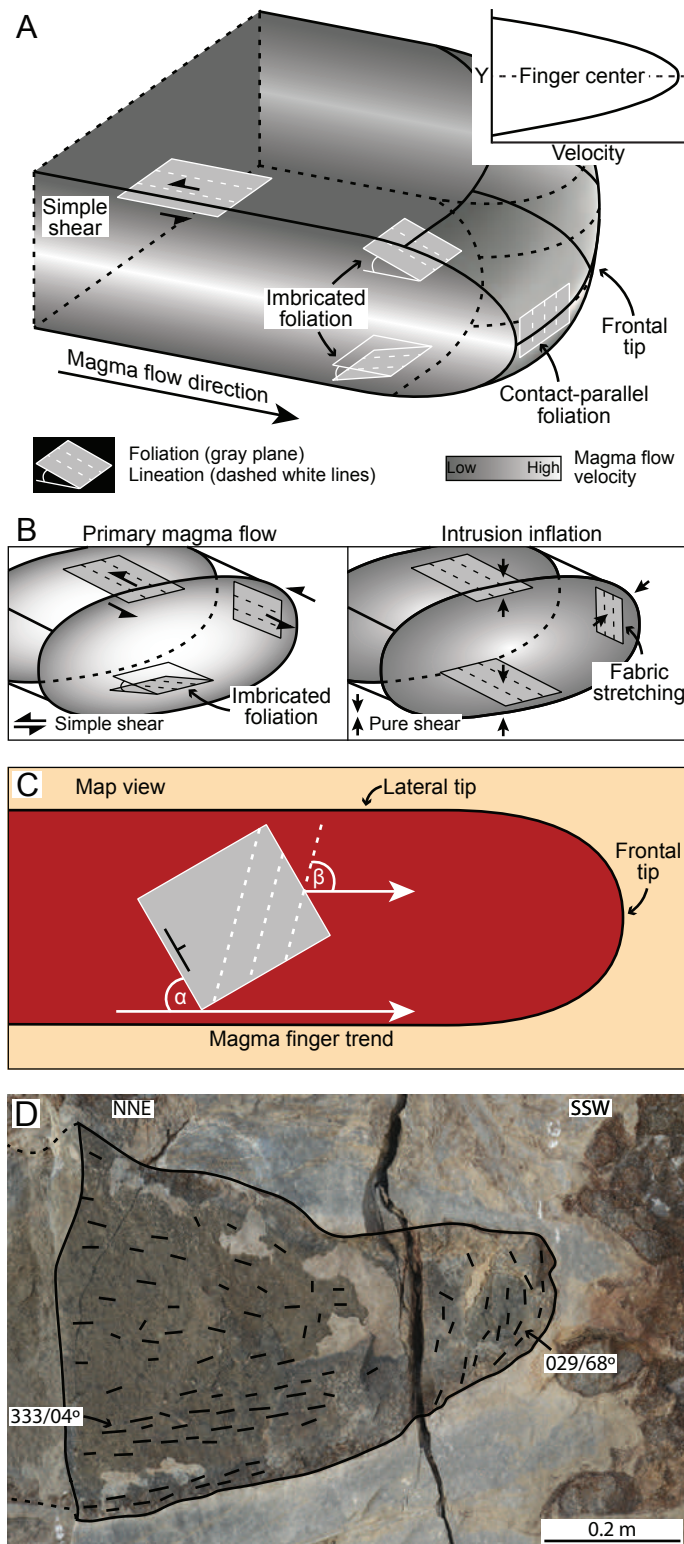


Figure 2: (A) Schematic diagram illustrates magma flow within igneous intrusions and highlights potential flow fabrics (modified after Magee et al., 2016). (B) Schematic diagrams illustrate expected fabrics resulted from primary magma flow and both vertical and horizontal magma finger inflation. (C) Schematic diagram shows the angular relation between both the foliation and lineation and the trend of magma fingers; α defines the angle between the foliation

strike and the magma finger trend, and β defines the angle between the lineation and the magma finger trend. (D) Field photograph of a lateral magma finger tip located at the SE margin of the Shonkin Sag laccolith (Montana, USA). Black lines indicate the **maximum** shape preferred orientation of clinopyroxene phenocrysts and show the alignment of minerals sub-parallel to the intrusion-host rock contact.

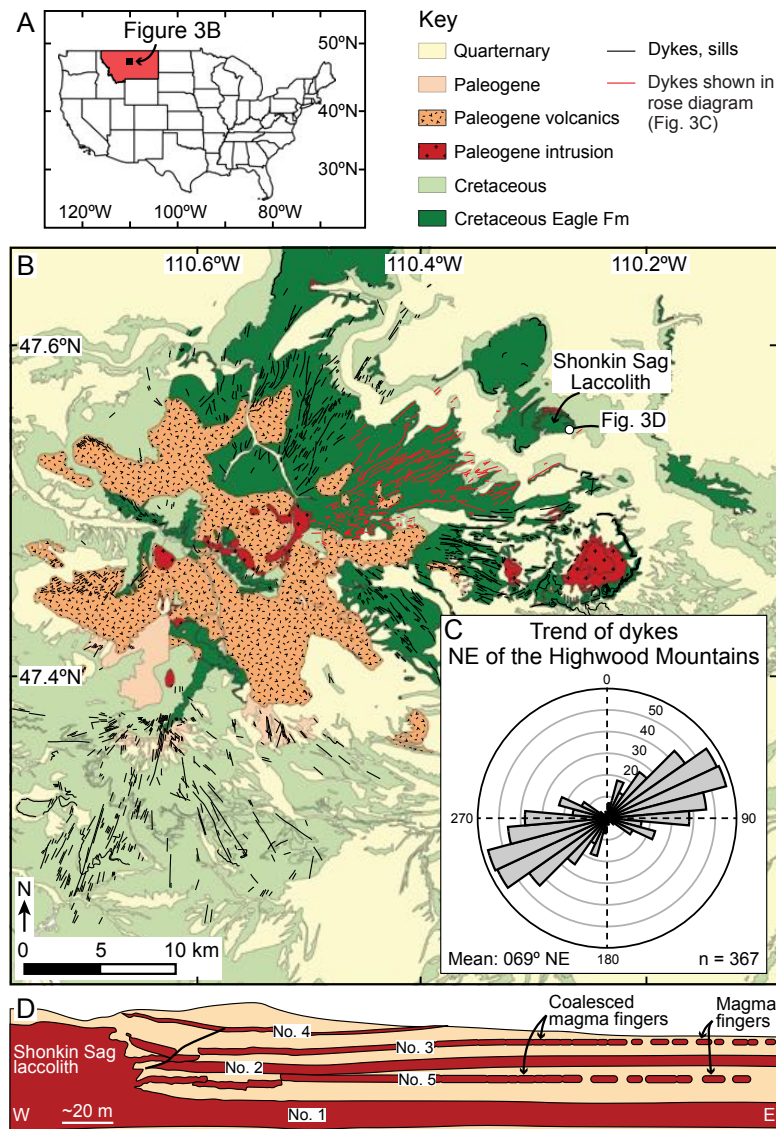


Figure 3: Location maps of study area. (A) Overview map shows the location of the Highwood Mountains, Montana, USA. (B) Simplified geological map indicates sedimentary, volcanic, and igneous rocks of the Highwood Mountains (based on the Geological Map of the quadrangles ‘Fort Benton’ and ‘Belt’; 1:100,000 scale; available from the Montana Bureau of Mines and Geology (2021)). Field examples of magma fingers are shown in Figures 1B and 1C. (C) Rose diagram shows the trend of dykes that crop out NE of the Highwood Mountains (color-coded in red in Figure 3B). (D) Schematic diagram of a cliff face located at the southeast Shonkin Sag laccolith margin shows the transition of the laccolith into 5 emerging sills. Sills No. 3 and No. 5 show evidence of both coalesced and discrete magma fingers. Note that magma fingers indicated in the **cross section** are schematic and do not represent the accurate size or

location. Sample locations and drone imagery of the outcrop are provided in Supplemental Material S1–S2. The cross section location is indicated in Figure 3B.

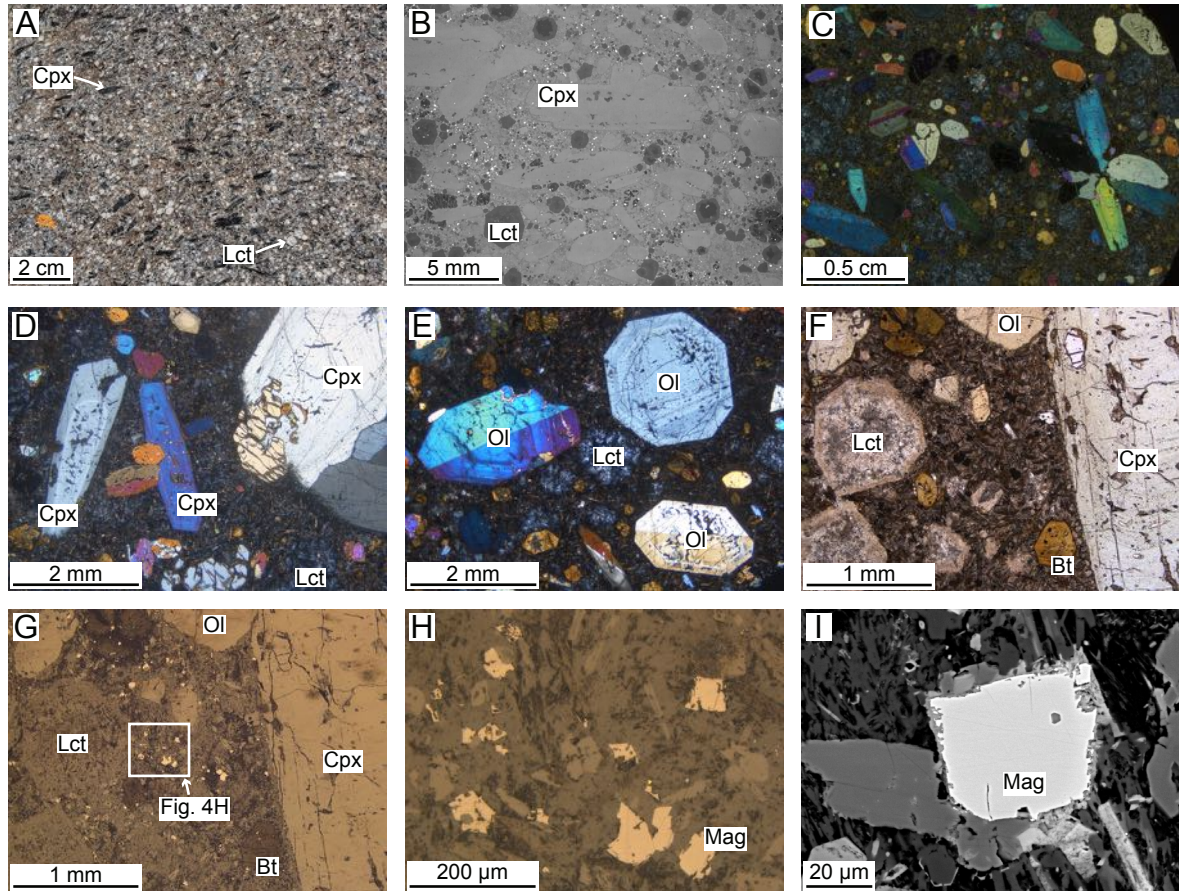


Figure 4: (A) Field photograph and (B) HRXRCT scan of shonkinite from magma fingers at the SE Shonkin Sag laccolith margin. Note the shape preferred orientation of Cpx. Cpx–clinopyroxene; Lct–leucite. (C–H) Photomicrographs of shonkinite under (C–E) crossed-polarized light, (F) plane-polarized light, and (G, H) reflected light. Ol–olivine; Bt–biotite; Mag–magnetite. (I) Backscattered electron image of a magnetite grain. Note that two images with different brightness-level were merged to visualize the internal magnetite structure and the groundmass. Raw-images are shown in the Supplemental Material S5.

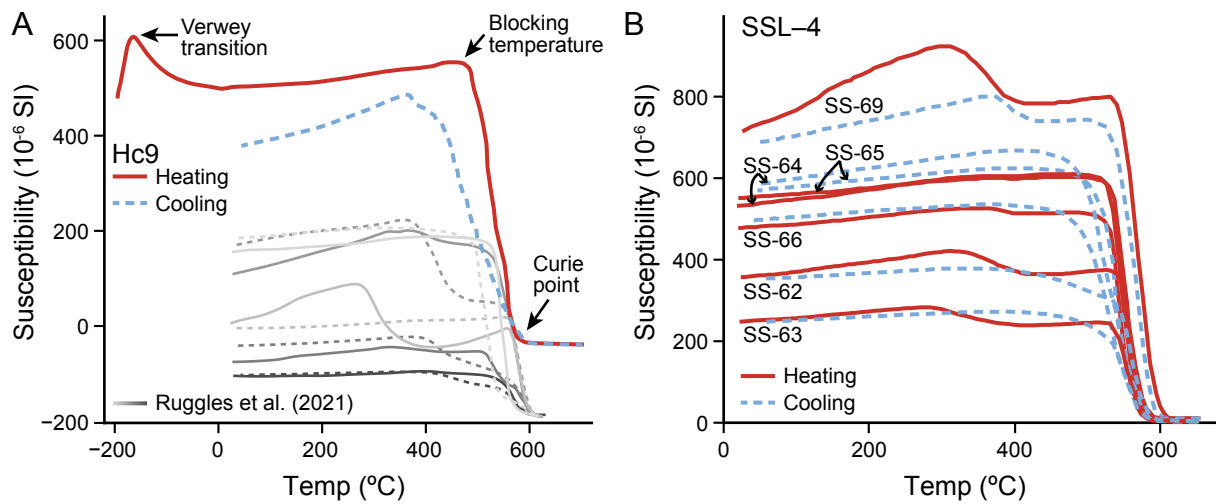


Figure 5: Low-to-high temperature, low-field susceptibility experiment of (A) sample Hc9 collected within magma finger Hc and (B) samples collected along a transect through the Shonkin Sag laccolith (SSL-4). Arrows in (A) indicate the Verwey transition (-165 $^{\circ}\text{C}$), blocking temperature (483 $^{\circ}\text{C}$), and the Curie point (570 $^{\circ}\text{C}$). Gray lines in (A) show data from samples collected from the Shonkin Sag laccolith and emerging sills as presented by Ruggles et al. (2021). Continuous and dashed lines indicate heating and cooling curves, respectively. (B) Specimens of sample group SSL-4 have blocking temperatures at about 520–530 $^{\circ}\text{C}$ and Curie points occur between 580–605 $^{\circ}\text{C}$.

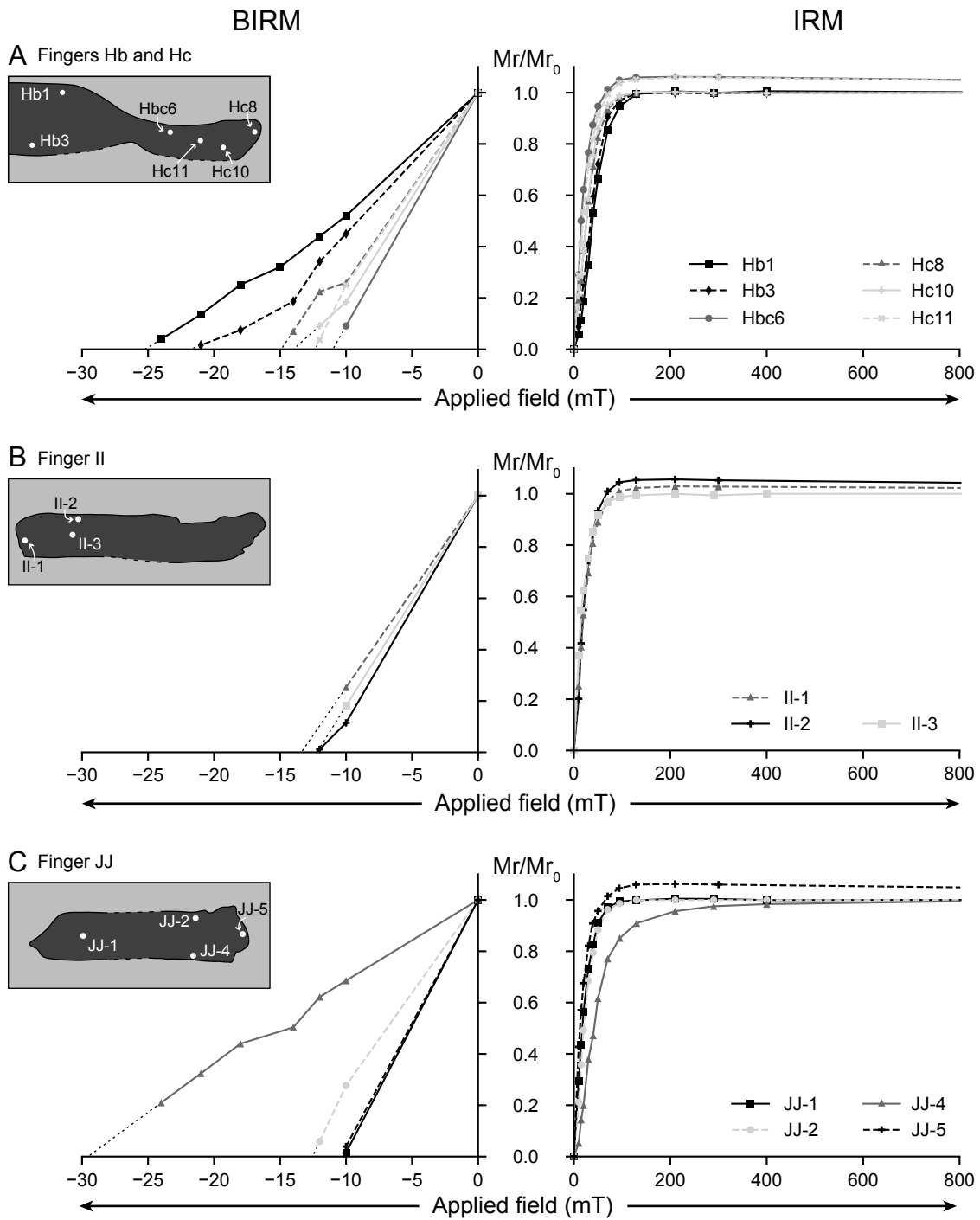


Figure 6: Results of isothermal remanent magnetization (IRM) and back-field IRM (BIRM) demagnetization experiments for samples in (A) fingers Hb and Hc, (B) finger II, and (C) finger JJ. Black dashed lines in BIRM plots are extrapolated BIRM curves which are used to estimate the coercivity of remanence (H_{CR}). Schematic diagrams of magma fingers indicate the sample location (white dots).

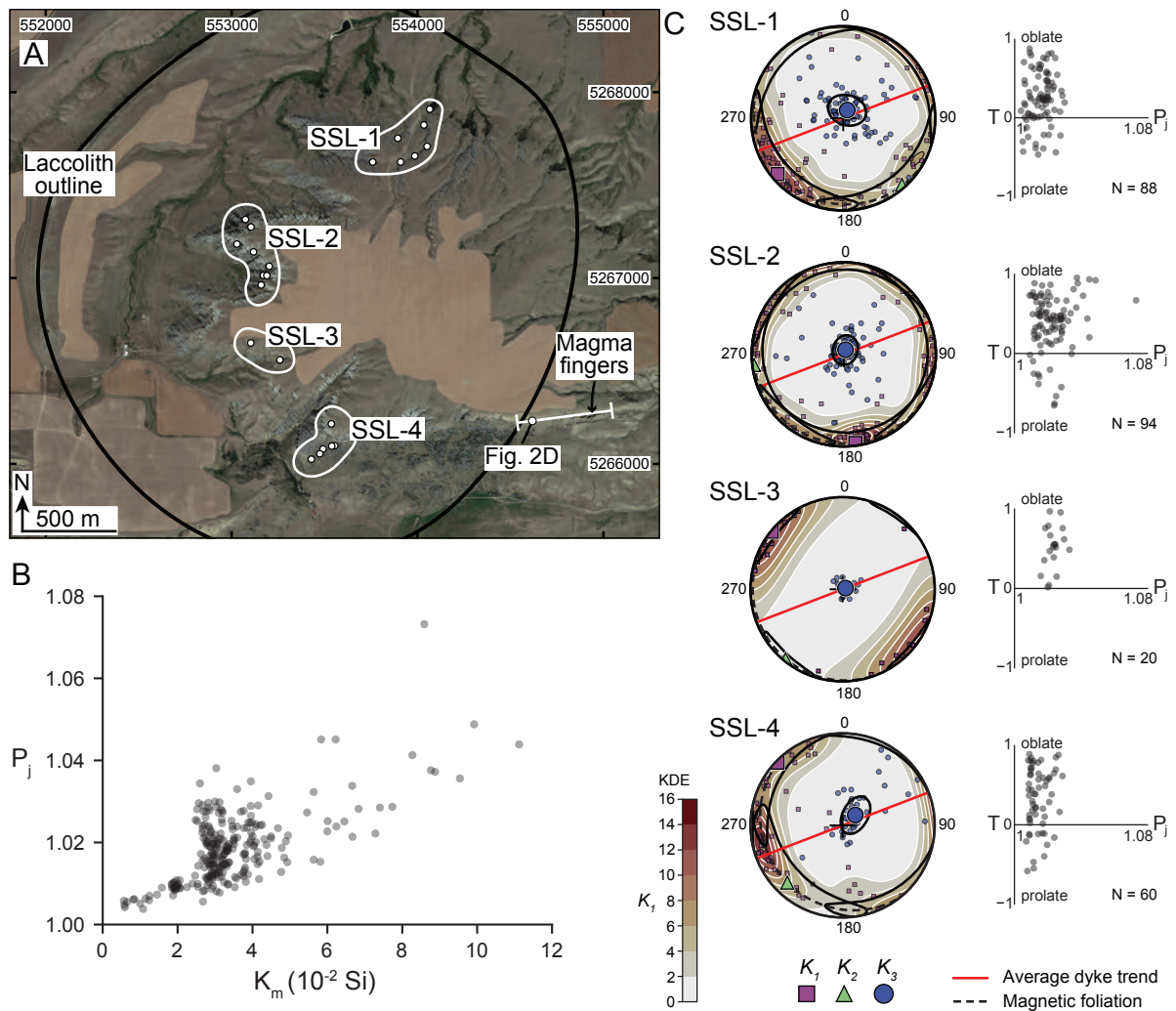


Figure 7: (A) Satellite image (GoogleEarth) of the Shonkin Sag laccolith shows the sample locations of sample group SSL-1–SSL-4 (white dots) and the location of magma fingers at the SE laccolith margin; laccolith outline after Hurlbut Jr. (1939). (B) Plot of the mean magnetic susceptibility (K_m) against the corrected degree of anisotropy (P_j) for all specimens. (C) Equal-area lower hemisphere stereonet plots of the anisotropy of magnetic susceptibility (AMS) for the four sample groups. 95% confidence ellipses are plotted for the average principal susceptibility axes. **Orientation density distribution contours are visualized for K_1 axes.** Red lines indicate the average trend (069° NE) of dykes NE of the Highwood Mountains, as is shown in Fig. 2C. P_j is plotted against the shape parameter (T) for each sample group.

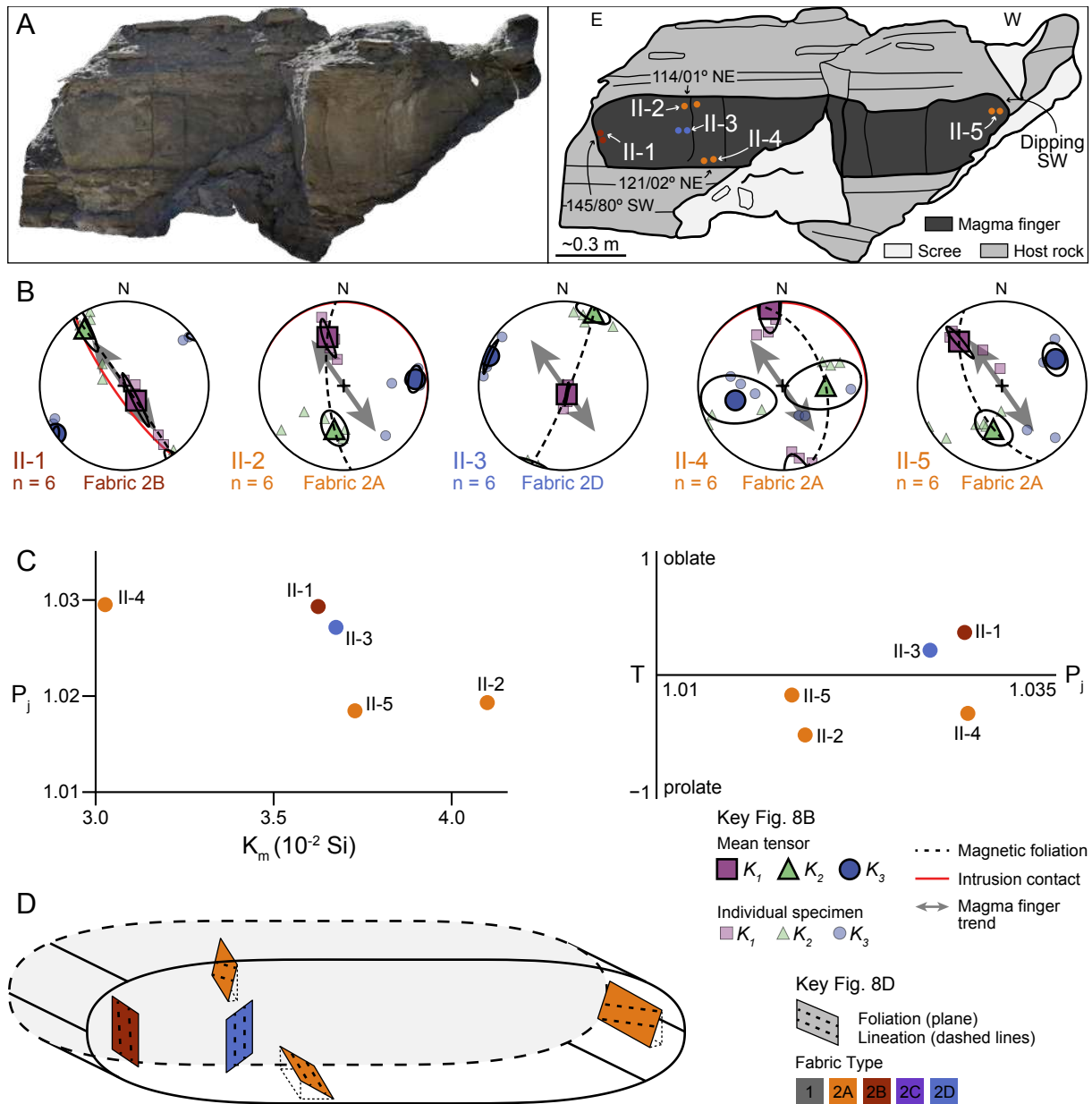


Figure 8: (A) Photomosaic and interpreted sketch for magma finger II. Dots are color-coded for the fabric type and highlight the individual sample locations, and structural measurements (strike/dip) indicate the intrusion-host rock contact. (B) Equal-area, lower hemisphere stereonet plots of the anisotropy of magnetic susceptibility (AMS) for the five sample locations (II-1–II-5) shown in (A). 95% confidence ellipses are plotted for the average principal susceptibility axes. The magma finger trend (145° SE; gray arrow) is inferred from the intrusion-host rock contact at the lateral E finger tip (145/80° SW). (C) Plots for the corrected degree of anisotropy (P_j) against both the mean magnetic susceptibility (K_m) and the shape factor (T). Note that the plotted measurements are mean values for each sample location in finger II. (D) Schematic

diagram shows the magnetic fabric orientation at the approximate sample location within magma finger II.

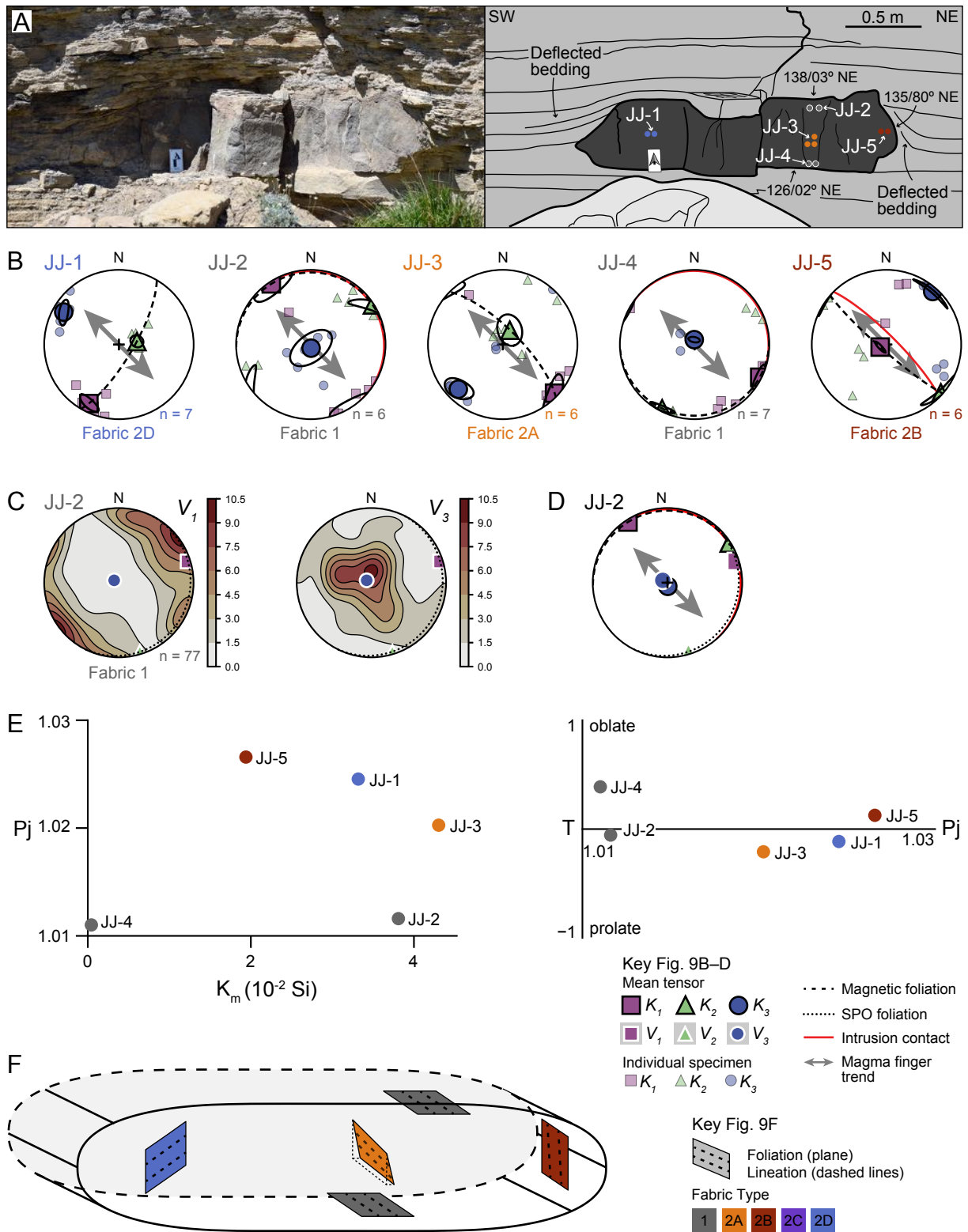


Figure 9: (A) Photograph and interpreted sketch for magma finger JJ. Dots are color-coded for the fabric type and highlight the individual sample locations, and structural measurements (strike/dip) indicate the intrusion-host rock contact. (B) Equal-area, lower hemisphere stereonet plots of the anisotropy of magnetic susceptibility (AMS) for the five sample locations (JJ-1–

JJ-5) shown in (A). 95% confidence ellipses are plotted for the average principal susceptibility axes. The magma finger trend (135° SE; gray arrow) is inferred from the intrusion-host rock contact at the lateral NE finger tip ($135/80^\circ$ NE). (C) Equal-area, lower hemisphere stereonet plots show the orientation density distribution of long axes (V_1) and short axes (V_3) orientations of clinopyroxene and olivine crystals in JJ-2; average fabric tensor axes orientations (V_1 , V_2 , V_3) are indicated. (D) Equal-area, lower hemisphere stereonet plot shows the comparison of AMS (K_1 , K_2 , K_3) and fabric tensor (V_1 , V_2 , V_3) axes orientations. (E) Plots for the corrected degree of anisotropy (P_j) against both the mean magnetic susceptibility (K_m) and the shape factor (T). Note that the plotted measurements are mean values for each sample location in finger JJ. (F) Schematic diagram shows the magnetic fabric orientation at the approximate sample location within magma finger JJ.

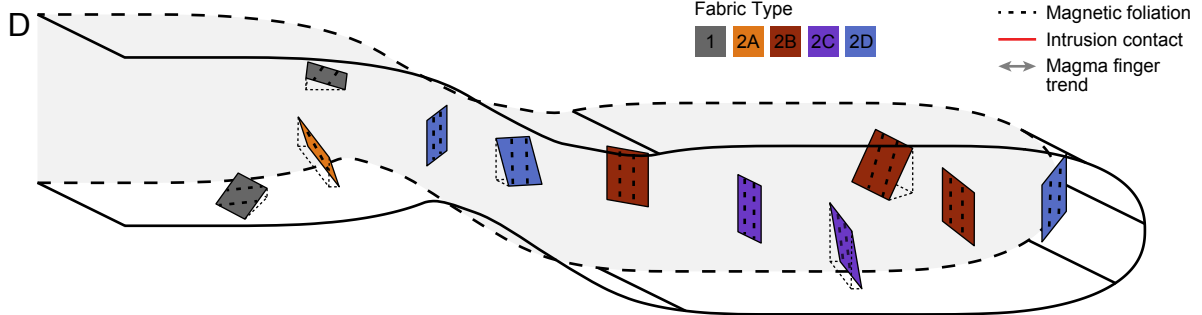
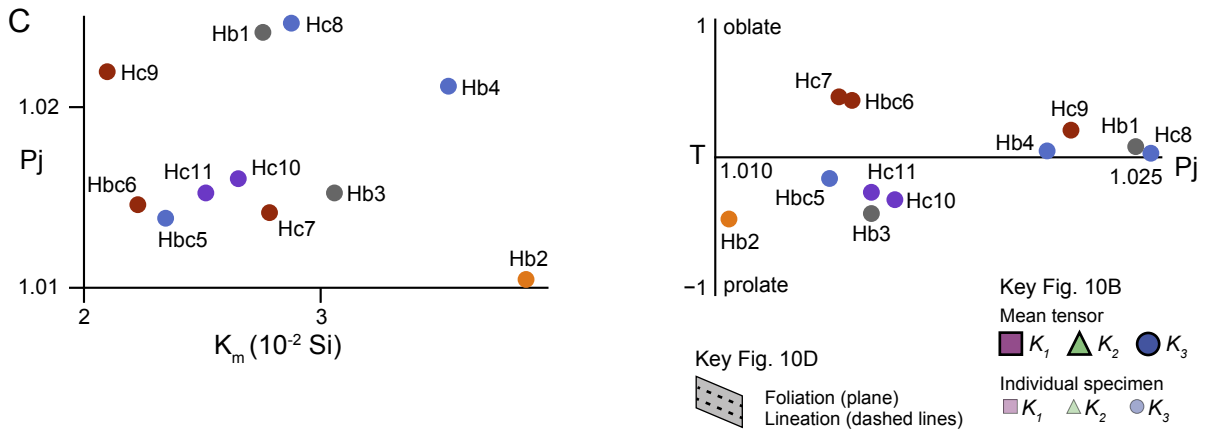
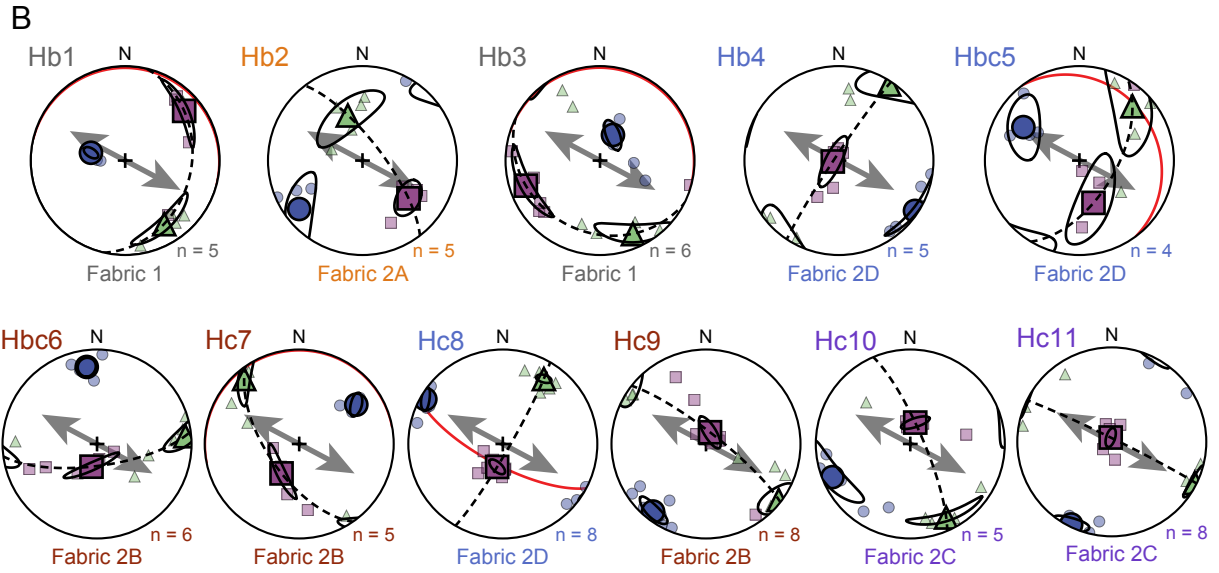
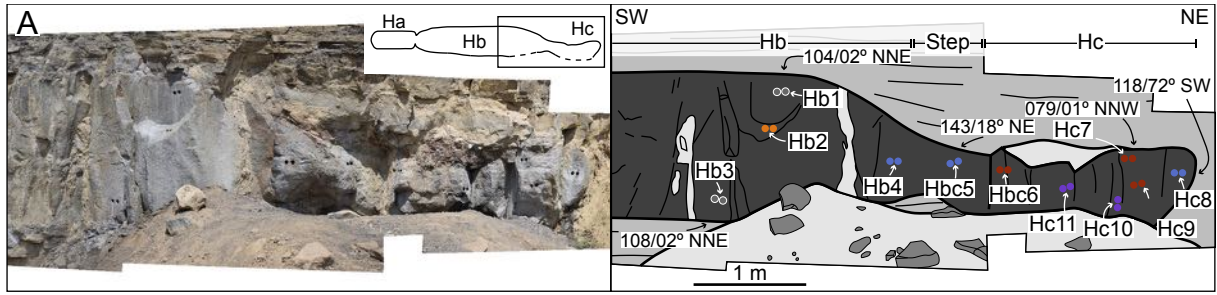


Figure 10: (A) Photomosaic and interpreted sketch for magma fingers Hb and Hc. Dots are color-coded for the fabric type and highlight the individual sample locations, and structural measurements (strike/dip) indicate the intrusion-host rock contact. (B) Equal-area, lower hemisphere stereonet plots of the anisotropy of magnetic susceptibility (AMS) for the eleven sample locations (Hb1–Hc11) shown in (A). 95% confidence ellipses are plotted for the average principal susceptibility axes. The magma finger trend (118° SE; gray arrow) is inferred from the intrusion-host rock contact at the lateral NE finger tip of Hc ($118/72^{\circ}$ SW). (C) Plots for the corrected degree of anisotropy (P_j) against both the mean magnetic susceptibility (K_m) and the shape factor (T). Note that the plotted measurements are mean values for each sample location in fingers Hb and Hc. (D) Schematic diagram shows the magnetic fabric orientation at the approximate sample location within the coalesced magma fingers Hb and Hc.

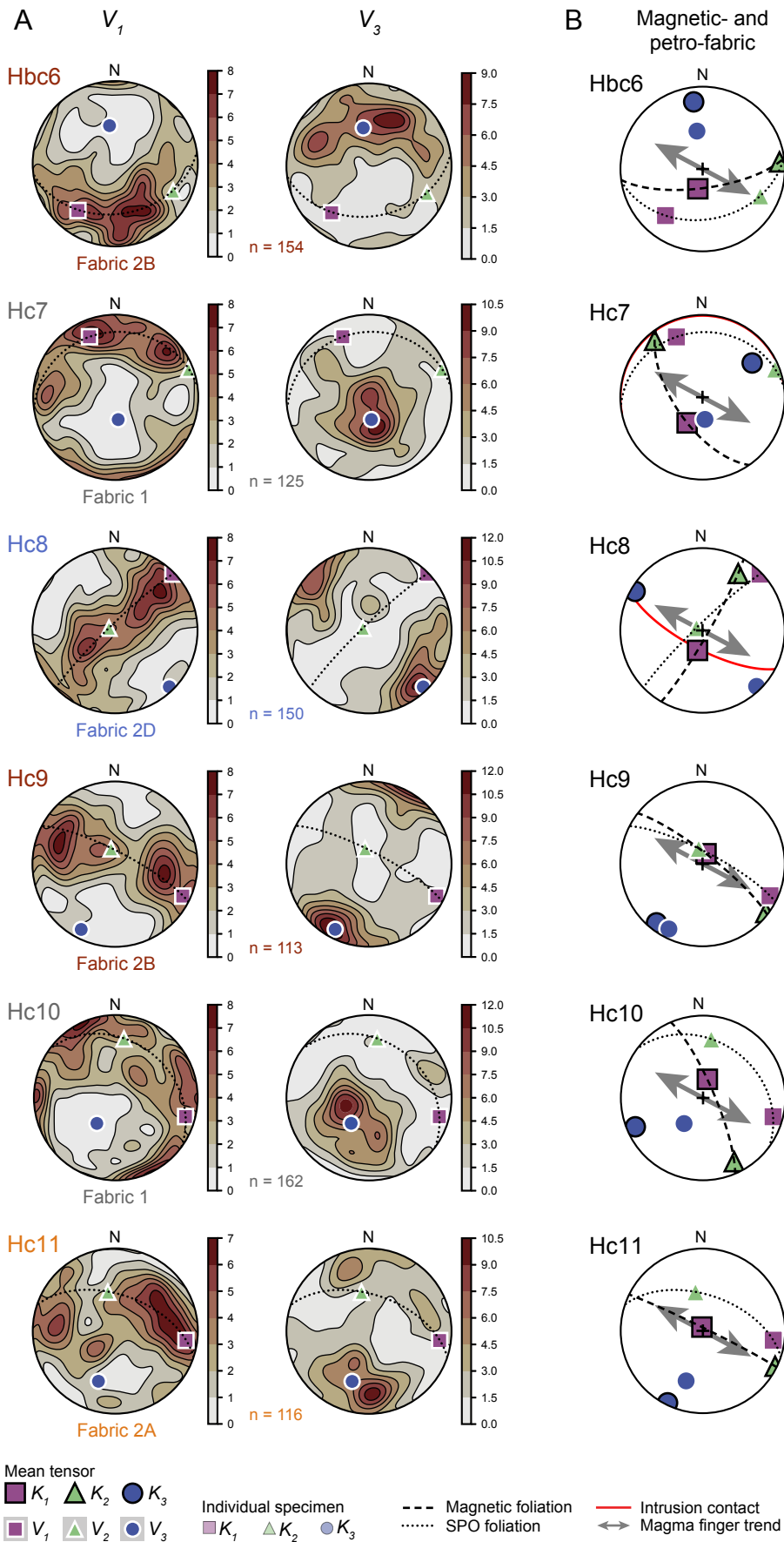


Figure 11: (A) Equal-area, lower hemisphere stereonet plots show the orientation density distribution of long axes (V_1) and short axes (V_3) orientations of clinopyroxene and olivine crystals for one sample in the intrusive step (Hbc6) and for finger Hc (Hc7–Hc11); average petrofabric tensor axes orientations (V_1, V_2, V_3) are indicated. (B) Equal-area, lower hemisphere stereonet plots show the comparison of AMS (K_1, K_2, K_3) and petrofabric tensor (V_1, V_2, V_3) axes orientations.

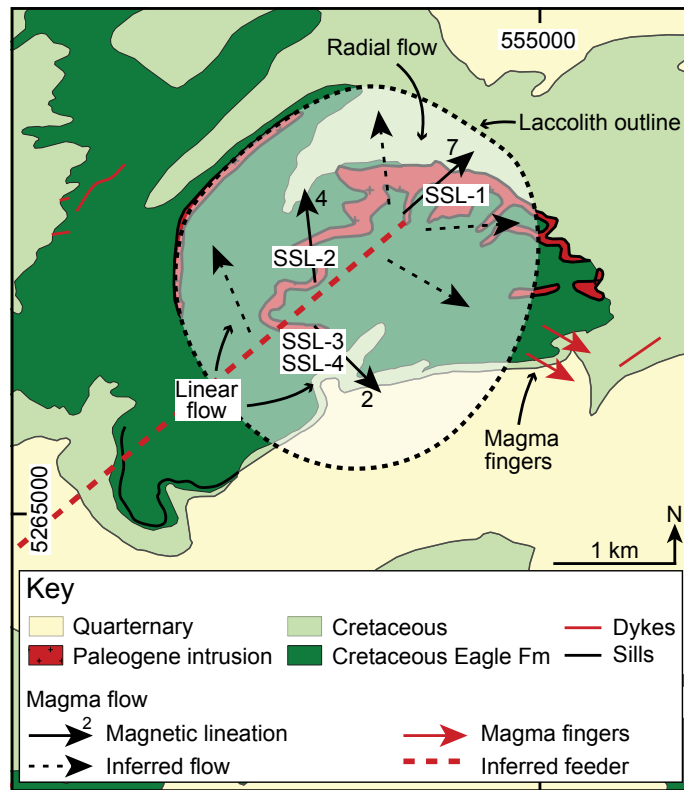


Figure 12: Simplified geological map of the Shonkin Sag laccolith shows the potential feeder-dyke location, magnetic lineation orientations, and inferred magma flow pathways. The plunge of magnetic lineations is indicated at the tip of solid black arrows. The geological map is based on the quadrangle 'Fort Benton' (1:100,000 scale) available from the Montana Bureau of Mines and Geology (2021); laccolith outline after Hurlbut Jr. (1939).

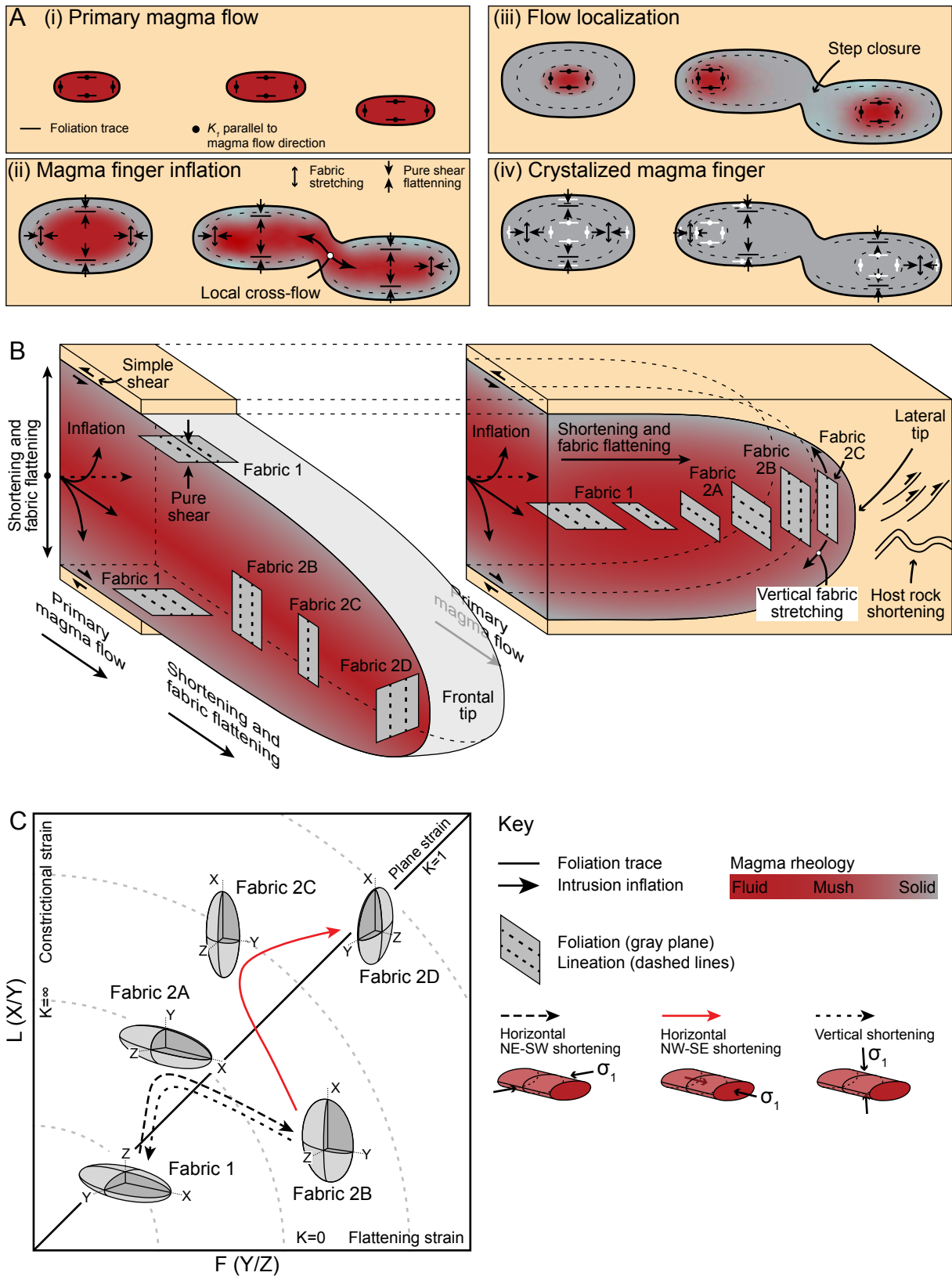


Figure 13: (A) Schematic cross-section diagrams show a time series of magma finger emplacement; cross sections are oriented perpendicular to both the magma finger long axis and the primary magma flow direction. Magma flow and emplacement processes and the expected

associated fabrics are indicated. Note that changing magma flow dynamics and local magma solidification can result in adjacent fabrics that are not directly related (iv). (B) Schematic 3-D diagram shows all fabric types as observed in the magma fingers studied, their spatial occurrence, and how they may develop over time. Magma flow processes such as primary flow, inflation, and fabric stretching/flattening are indicated. (C) Schematic Flinn diagram shows interpreted strain paths and fabric overprinting due to primary magma flow and both horizontal and vertical inflation.

Table 1: *Petrofabric analyses results*

SPO: Cpx and Ol

Sample	n	V_1		V_2		V_3		Foliation			P_j	T	Contact to host rock			α (°)	β (°)	Fabric
		Dec. (°)	Pl. (°)	Dec. (°)	Pl. (°)	Dec. (°)	Pl. (°)	Strike (°)	Dip (°)	Dip dir.			Strike (°)	Dip (°)	Dip dir.			
JJ-2	77	073	04	163	04	296	84	026	06	SE	2.657	0.38	138	03	NE	71	62	Fabric 1
Hbc6	154	219	28	115	24	351	52	081	38	S	2.047	0.45	-	-	-	37	79	Fabric 2B
Hc7	125	337	21	069	06	174	68	084	22	N	2.228	0.58	079	01	NNW	34	39	Fabric 1
Hc8	150	046	02	295	83	136	06	046	84	NW	2.669	0.52	118	72	SW	72	72	Fabric 2D
Hc9	113	115	10	346	74	207	12	117	78	NE	3.209	0.39	-	-	-	1	3	Fabric 2B
Hc10	162	105	13	008	29	217	58	127	32	NE	2.603	0.78	-	-	-	9	13	Fabric 1
Hc11	128	098	15	349	50	199	36	109	54	NNE	1.900	-0.10	-	-	-	9	20	Fabric 2A

DA: oxides

Sample	n	λ_1		λ_2		λ_3		Foliation			P_j	T
		Dec. (°)	Pl. (°)	Dec. (°)	Pl. (°)	Dec. (°)	Pl. (°)	Strike (°)	Dip (°)	Dip dir.		
JJ-2	8746	036	18	300	16	171	66	081	24	N	1.112	-0.63
Hbc6	2271	051	36	222	54	318	04	048	86	SE	1.122	0.04
Hc7	2660	158	68	039	11	305	19	035	71	SE	1.151	-0.27
Hc8	8980	312	88	049	00	139	02	049	88	NW	1.034	0.22
Hc9	4241	300	02	046	81	209	09	119	81	NE	1.089	-0.06
Hc10	2843	015	15	107	06	218	73	128	17	NE	1.124	-0.04
Hc11	364	041	47	164	27	272	31	002	59	E	1.240	0.06

Note: SPO–shape preferred orientation; DA–distribution anisotropy; n–number of analyzed grains; Dec.–declination; Pl.–plunge; Dip dir.–dip direction; P_j –corrected degree of anisotropy; T–shape parameter. Measurements are collected from one representative specimen of each sample.

Table 2: Anisotropy of magnetic susceptibility results

ip-AMS

Group & Sample ID	n	K_1		K_2		K_3		Magnetic foliation			K_m 10 ⁻² SI	P_j	T	Contact to host rock			α (°)	β (°)	Fabric
		Dec. (°)	Pl. (°)	Dec. (°)	Pl. (°)	Dec. (°)	Pl. (°)	Strike (°)	Dip (°)	Dip dir.				Strike (°)	Dip (°)	Dip dir.			
SSL-01	88	229	07	139	03	026	82	116	08	SSW	2.78	1.016	0.25	-	-	-	-	-	Fabric 1
SSL-02	94	173	04	263	02	019	86	109	04	SSW	4.31	1.023	0.39	-	-	-	-	-	Fabric 1
SSL-03	20	309	01	219	02	065	87	155	03	SW	3.86	1.023	0.52	-	-	-	-	-	Fabric 1
SSL-04	60	314	02	224	14	052	75	142	15	SW	2.84	1.014	0.34	-	-	-	-	-	Fabric 1
II-1	6	142	72	325	18	235	01	145	89	NE	3.63	1.029	0.35	145	80	SW	0	3	Fabric 2B
II-2	6	342	39	192	47	085	16	175	74	WSW	4.10	1.019	-0.49	114	01	NE	30	17	Fabric 2A
II-3	6	157	81	023	06	292	06	022	84	E	3.68	1.027	0.20	-	-	-	57	12	Fabric 2D
II-4	6	350	09	090	48	253	41	163	49	E	3.03	1.030	-0.31	121	02	NE	18	25	Fabric 2A
II-5	6	316	28	191	47	063	30	153	60	SW	3.73	1.018	-0.16	-	-	-	8	9	Fabric 2A
JJ-1	7	207	12	080	70	300	15	030	75	SE	3.32	1.025	-0.11	-	-	-	75	72	Fabric 2D
JJ-2	6	327	03	057	02	176	86	086	04	N	3.80	1.012	-0.06	138	03	NE	49	12	Fabric 1
JJ-3	6	133	05	026	72	225	17	135	73	NE	4.30	1.020	-0.21	-	-	-	0	2	Fabric 2A
JJ-4	7	117	03	207	05	356	85	086	05	S	0.04	1.011	0.39	126	02	NE	49	18	Fabric 1
JJ-5	6	248	83	131	03	041	07	131	83	SW	1.94	1.027	0.13	135	80	NE	4	67	Fabric 2B
Hb1	5	050	20	148	22	283	60	013	30	E	2.76	1.024	0.08	104	02	NNE	75	68	Fabric 1
Hb2	5	129	37	342	48	233	17	143	73	NE	3.87	1.010	-0.45	-	-	-	25	11	Fabric 2A
Hb3	6	251	18	156	16	027	65	117	25	SW	3.06	1.015	-0.41	108	02	NNE	1	47	Fabric 1
Hb4	5	261	85	033	04	124	04	034	86	NW	3.54	1.021	0.05	-	-	-	84	37	Fabric 2D
Hbc5	4	162	51	044	21	301	32	031	58	SE	2.35	1.014	-0.15	143	18	NE	87	44	Fabric 2D
Hbc6	6	194	70	085	07	352	19	082	71	S	2.23	1.015	0.41	-	-	-	36	76	Fabric 2B
Hc7	5	211	60	320	11	055	27	145	63	SW	2.78	1.014	0.44	079	01	NNW	27	87	Fabric 2B
Hc8	8	194	70	032	19	300	06	030	84	SE	2.88	1.025	0.03	118	72	SW	88	76	Fabric 2D
Hc9	8	019	79	127	03	218	10	128	80	NE	2.10	1.022	0.20	-	-	-	10	81	Fabric 2B
Hc10	5	013	71	154	15	247	11	157	79	NE	2.65	1.016	-0.31	-	-	-	39	75	Fabric 2C
Hc11	8	345	86	116	03	206	03	116	87	NE	2.51	1.015	-0.25	-	-	-	2	47	Fabric 2C

Note: AMS–anisotropy of magnetic susceptibility; n–number of analyzed specimens; Dec.–declination; Pl.–plunge; Dip dir.–dip direction; K_m –average magnetic susceptibility; P_j –corrected degree of anisotropy; T–shape parameter. Presented measurements are group/sample mean data.